Building and Environment 196 (2021) 107774

Contents lists available at ScienceDirect

Building and Environment

journal homepage: http://www.elsevier.com/locate/buildenv

Modeling specular transmission of complex fenestration systems with data-driven BSDFs

Gregory J. Ward [a], Taoning Wang [b], David Geisler-Moroder [c], Eleanor S. Lee [b,*], Lars O. Grobe [d], Jan Wienold [e], Jacob C. Jonsson [b]

[a] Anyhere Software, 950 Creston Road, Berkeley, CA, 94708, USA
[b] Building Technologies and Urban Systems Division, Energy Technologies Area, Lawrence Berkeley National Laboratory (LBNL), Mailstop 90-3147, 1 Cyclotron Road, Berkeley, CA, 94720, USA
[c] Bartenbach GmbH, Rinner Strasse 14, 6071, Aldrans, Austria
[d] Lucerne University of Applied Sciences and Arts (HSLU), Technikumstrasse 21, 6048 Horw, Switzerland
[e] Ecole Polytechnique Fédérale de Lausanne (EPFL), ENAC IA LIPID LE 1 111 (Bâtiment LE), Station 18, CH-1015, Lausanne, Switzerland

ARTICLE INFO

Keywords:
Bidirectional scattering distribution function
Daylighting
Complex fenestration systems
Windows
Building energy efficiency
Discomfort glare

ABSTRACT

A Bidirectional Scattering Distribution Function (BSDF) describes how light from each incident direction is scattered (reflected and transmitted) by a simple or composite surface, such as a window shade. Compact, *tabular* BSDFs may be derived via interpolation, discretization and/or compression from goniophotometer measurements. These *data-driven* BSDFs can represent any measurable distribution to the limits of their tabulated resolution, making them more general than parametric or analytical BSDFs, which are restricted to a particular class of materials. However, tabulated BSDFs present a trade-off between higher sampling loads versus lower directional accuracy during simulation. Low-resolution BSDFs (e.g., Klems basis) may be adequate for calculating solar heat gains but fall short when applied to daylight glare predictions. The tensor-tree representation moderates this trade-off using a variable-resolution basis, providing detail where needed at an acceptable cost. Independently, a *peak extraction* algorithm isolates direct transmission from any tabular BSDF, enabling high-resolution beam radiation and glare analysis through transmitting systems with a "vision" component. Our data-driven BSDF methods were validated with a pilot study of a fabric shade installed in an outdoor, full-scale office testbed. Comparisons between measurement and simulation were made for vertical illuminance, specular and near-specular transmission, and daylight glare probability. Models based on high resolution BSDF measurements yielded superior results when accounting for anisotropy compared to isotropic models. Models with higher resolution produced more accurate source luminance data than low-resolution models. Further validation work is needed to better characterize generality of observed trends from this pilot study.

1. Introduction

There are a wide variety of window shading and daylighting materials and systems – venetian blinds, fabric roller shades, films, awnings, expanded metal mesh, fritted and patterned glass – that affect the intensity and distribution of incoming solar radiation and daylight in buildings. Advanced materials R&D have investigated complex structures at micro- and nanoscales to improve energy efficiency [1]. Microprismatic films and macroscopic louvers provide daylight redirection to the core of sidelit perimeter zones. Z-pleated fabrics reflect direct solar radiation to the outdoors but admit diffuse daylight [2]. Angular selective films with inclined columnar nanostructures enable seasonal admission of sunlight for passive solar heating during the winter and solar occlusion during the summer [3]. Dynamic metamaterials with deformable prisms track and redirect sunlight over the course of the day [4]. Coatings, films, and laminates such as switchable transparent liquid crystal devices produce anisotropic properties that deviate from Fresnel angle-dependent models [5].

These optically complex fenestration systems (CFS) affect window heat gains, daylight, thermal and visual comfort, and view. They can be used as a retrofit measure or for new construction in both residential and commercial buildings and can thus help to reduce the 4.33×10^{18} J (4.2

* Corresponding author. Lawrence Berkeley National Laboratory, Berkeley, CA, USA.
E-mail addresses: gregoryjward@gmail.com (G.J. Ward), taoningwang@lbl.gov (T. Wang), David.Geisler-Moroder@bartenbach.com (D. Geisler-Moroder), eslee@lbl.gov (E.S. Lee), larsoliver.grobe@hslu.ch (L.O. Grobe), jan.wienold@epfl.ch (J. Wienold), JCJonsson@lbl.gov (J.C. Jonsson).

https://doi.org/10.1016/j.buildenv.2021.107774
Received 11 November 2020; Received in revised form 16 January 2021; Accepted 27 February 2021
Available online 11 March 2021

$\times 10^{15}$ Btus) or 3668 kWh per capita of primary energy use attributable to windows in the United States [6]. If operable and automated, fenestration systems are integrated with HVAC and lighting controls to enable demand responsive, grid-interactive buildings, increased use of renewable energy and reduction of carbon emissions may occur [7].

New calculation methods have been developed that enable speedy annual energy performance evaluations of CFS materials and systems. The methods use a multi-phase matrix approach where each phase of flux transfer from one discretized element to the next is pre-computed using ray tracing. Then, the total flux transfer is determined on a timestep basis using matrix multiplication [8–11]. For some methods, flux transfer through the fenestration layer is represented with a bidirectional scattering distribution function (BSDF) matrix, facilitating modeling of operable or dynamic shading and daylighting systems through substitution of the BSDF matrix without having to recompute the other matrices [12–18].

BSDF models developed for determining solar heat gains (e.g. Ref. [19]) utilize the Klems hemispherical basis which has low spatial resolution (i.e., exiting flux averaged over a 10–15° apex angle, 145 patches in the outgoing hemisphere). Consequently, flux from narrow sources is spread over a larger area and its intensity is reduced accordingly. This does not impact the calculation of integral solar heat gains, but can introduce a significant bias in predictions of visual comfort. The latter is impacted by highly directional scattering of light from narrow light sources; e.g., the deflection of sunlight or its specular or near-specular transmission without change of direction in and around the line of sight from the source. *High-resolution* models more accurately represent the intensity and peaky distribution of specular and redirected solar transmission. In this research, the resolutions are parameterized by hemispherical subdivision into $2^k \cdot 2^k$ patches of equal solid angle [20]; e.g., $k = 7$ corresponds to $2^{2\cdot7} = 16,384$ patches of solid angle 0.004 sr, or an average apex angle of 1.3°.

There are significant measurement and computational costs associated with generating such high-resolution models, deterring development of industry standards and production of a certified BSDF database. Analytical models that can be parametrized by a few, easily measurable properties have been produced for a subset of materials to meet urgent industry demands (see Section 2). Their development and validation are elaborate, and applicability is limited to the particular class of BSDFs and assumptions that they have been developed for. Data-driven modelling allows one to replicate arbitrary BSDFs and lends itself to bypass the elaborate development of analytical models [21], e.g., in the case of complex fenestration systems featuring highly irregular scattering properties, or as an intermediary representation that can guide the development and validation of analytical models addressing entire classes of BSDFs, e.g., of fabrics.

In this study, we present a general method for generating data driven BSDFs and results from validation of the method. We describe current methods used to measure and interpolate BSDF data. In light of instrument and computational constraints, a new peak extraction algorithm was developed to be used during time-step simulations to model specular and near specular transmission. The described methods were validated in an evaluation of a single roller shade fabric using laboratory and full-scale outdoor field measurements. This pilot evaluation provides insights into sources of error across the entire workflow and is illustrative of model performance. We discuss results and next steps to further develop methods for generating and using high-resolution BSDF data.

2. Background

2.1. Definition of BSDFs

Bidirectional scattering distribution functions describe transmission and reflection properties of a material or system for any pair of incident and exiting angles [22,23]. They can be tabulated to form discrete sets of values for a defined number and set of directions (i.e., incident and exiting patches). These directions can be defined by a regular grid of elements that subdivide the incoming and outgoing hemispheres into a series of solid angles or a grid of elements that is irregular and adaptive to the BSDF. Table 1 provides a summary of the various tabulated BSDF bases employed in building simulations with their respective angular resolutions. Appendix A explains the Radiance convention for phi and theta angles used in this manuscript and terms used to describe the scattering behavior of materials (i.e., anisotropic and isotropic).

2.2. State-of-the-art methods for generating tabulated BSDF models

For the five-phase method used to calculate indoor illuminance and luminance levels for annual simulations [15,16], there are two matrices required to represent the BDSF of the fenestration system: 1) a low-resolution transmission (T) matrix, where the source is a large-area patch of the subdivided sky hemisphere, and 2) a high-resolution coefficient matrix (C_{ds}), where the source is the orb of the sun. The tabulated BSDF data for the T and C_{ds} matrices can be generated using:

- evaluation of analytical models (e.g., Radiance material models based on fundamental physics; examples of use given in Refs. [24,25]) or other parametric models that can be mathematically described and fit to measured data (e.g. Ref. [26]), or
- ray-tracing tools (e.g., *genBSDF* [27]), or
- data-driven modelling, e.g., interpolation of measured BSDFs, which is the focus of this research.

Table 1
Resolution of various tabulated BSDF angle bases.

Angle basis	Resolution: Number of subdivisions per incoming × outgoing hemisphere	Average patch size cone with apex angle (°)	Patch size: average solid angle (sr) per subdivision (2π/subdivisions)	N, where sun (0.533° orb) intensity is N times less than reality
Klems [12]	145 × 145	13.5°	0.043000	641[b]
IEA SHC Task 21 [28]	145 × 1297	10–15° incident and 5° exiting	0.004800	253–792
Tensor tree[a]	$2^{2\cdot k} \times 2^{2\cdot k}$			
	k = 5, 1024 × 1024	5.06°	0.006136	90.3
	k = 6, 4096 × 4096	2.53°	0.001534	22.6
	k = 7, 16,384 × 16,384	1.27°	0.000383	5.6
	k = 8, 65,536 × 65,536	0.63°	0.000096	1.4
	k = 9, 262,144 × 262,144	0.32°	0.000024	0.4
	k = 10, 1,048,576 × 1,048,576	0.16°	0.000006	0.1

[a] Initial resolution before data-reduction to a four-dimensional, compact, tensor tree structure.
[b] For the Klems BSDF basis with an average apex angle of no smaller than 13.5°, flux from the 0.533° orb of the sun is spread out by a square of that ratio, or about a factor of 641 than it would be in reality if unscattered; i.e., 2.5×10^6 cd/m^2 versus 1.6×10^9 cd/m^2 for luminance.

Tabulated BSDFs can be produced for any angular basis and resolution (e.g., Klems or tensor tree). Accuracy of the BSDF matrices, T and C_{ds}, is therefore dependent on the accuracy of the underlying models and measured data that describe the scattering behavior of the fenestration system. For all other modeling methods that render the direct sun component (e.g., *rtrace* and *rpict* in Radiance [29]), the same principle holds true.

So it behooves the end user to critically examine the underlying *source* of the tabulated BSDF in order to avoid errors in simulated performance. For the Radiance *glass* material type,[1] for example, angular dependency is modeled using Fresnel equations, glass transmissivity, and index of refraction; intensity reductions are modeled but not the change in direction due to refraction. The underlying model is continuous, requires no interpolation, and specular transmission is accurately modeled to the extent that the refractive properties of the glass are determined properly. For other material types, such as *transfunc, transdata, brightfunc, brightdata, or BRTDfunc*, there are built-in limitations, i.e., specular transmission or reflection is modeled as purely specular, similar to glass, where a 0.5° sun source is rendered as a 0.5° source on the window with no near-specular scattering and where reflected light off adjacent buildings is not taken into account. A review of current methods of generating tabulated BSDFs is given in Refs. [30,31].

The *genBSDF* tool [27] relies on a geometrical description of the CFS material or system and inputs describing the properties of the materials, and thus may not reflect variations in the final manufactured product. *genBSDF* does not explicitly model specular or reflected peaks: rays are traced between input and output patches (solid angles), so the maximum resolution of the C_{ds} matrix is set by the size of the solid angles. To represent the 0.533° apex angle of the sun disc, for example, the BSDF basis would need to have a resolution of k = 9 (see Table 1). Generating an anisotropic tensor tree model with k = 7 (16,384 data points per hemisphere) is already computationally demanding (and sometimes infeasible) in terms of time and memory.

Irrespective of the origin of the underlying data, the increased accuracy of such refined models can be leveraged only if the tabular BSDF is sampled at adequate resolution at the rendering stage. For systems with a pure (direct) transmitted component, a high-resolution tensor tree will not capture spatial variation in the system. To overcome this limitation and avoid the memory needs of sampling a highly directional BSDF, a geometric model of the shading device may be embedded using *genBSDF* ("proxy geometry", e.g., louvers of a venetian blind). The accurate modeling of peaks by specular reflection and transmission is then ensured by the backward ray-tracing algorithm and independent from the stochastically sampled tabular BSDF and its resolution. A tabular BSDF of reduced directional resolution may then account for deflected light in the diffuse interreflection calculation.

In summary, for certain materials and systems, tabulated BSDFs for the T and C_{ds} matrices can be generated with reasonable confidence. These include dielectric materials and CFS with opaque elements and micro- and macroscopic geometry (e.g., Venetian blinds with opaque matte painted slats; matte perforated metal screens where diffraction can be ignored). For many other materials and systems, general methods for generating tabular BSDF need to be developed and validated.

3. Methods for generating and using tabulated BSDFs from measured data

In this section, we describe a general method for generating tabulated BSDFs from measured goniophotometer data and using the BSDFs in simulations, with a focus on accurate measurement and modeling of specular and near-specular transmission. The overall workflow (Fig. 1) involves the following steps, which are discussed in detail in the following subsections:

1. Measure the light scattering properties of a sample using a goniophotometer;
2. Derive interpolants from measured goniophotometer data then generate and compress the tabulated BSDFs;
3. Generate point-in-time illuminance and scene images using the five-phase or other methods with peak extraction.

3.1. Goniophotometer measurements

Two fundamental techniques to measure the angular distribution of scattering can be distinguished. Imaging goniophotometers relate positions on a pixel array to the scattering direction through refractive or reflective optics, and can instantaneously capture multiple data-points or entire distributions. Krehel et al. [32] however found that the large beam diameter and lower resolution data acquired from an imaging goniophotometer limit their accuracy in the case of specular scattering. Scanning goniophotometers typically achieve a higher dynamic range and angular resolution. They sample the distribution sequentially by movement of detector, sample and light source. A detailed review of the capabilities of various types of goniophotometers is given in Refs. [33–35].

In this study, scanning goniophotometers are employed (i.e., Model "pgII", Pab Advanced Technologies Ltd [36,37]). The instrument's dynamic range of $1{:}10^7$ and the capability to refine the resolution for selected regions of interest, allows one to measure both peak and diffuse background intensities at adaptive directional resolution. The chosen combination of a full spherical scan with a refinement in regions of specular transmission or reflection leads to datasets comprising more than 100,000 points per exiting hemisphere and incident direction (Fig. 2). The configuration of the goniophotometers is not optimized for a particular class of samples, but rather balances support of a wide range of sample properties; e.g., in terms of structure size and dimensions, resolution, and acquisition time. In this research, this limits the resolution of the specular and near specular transmission.

The configuration of the illuminator defines the collimation and the beam diameter on the sample. Since the field of view of the detectors exceeds the sample size, this diameter is equal to the sampling aperture. The measured BSDF is an average over this aperture, which has to be sufficiently large to be representative of the sample. In the case of large-scale features, the illuminating beam can cover a maximum area of about 70 mm in diameter.[2]

The apparent size of the light source in the measurement and the size of the illuminated area on the sample are interdependent, since both are controlled by the position of the focus lens. To illustrate, beam profiles of three typical configurations of the illuminator with different positions of the focus lens in the beam path are given in Fig. 3, with examples of corresponding measured data given in Fig. 4:

- *Focus on infinity.* This configuration produces a beam profile that is closest to "parallel light". A large area on the sample is illuminated (diameter is approximately 65 mm for normal, perpendicular illumination). This averages out the local effects of large structures or inhomogeneities. The beam's full-width-half-maximum (FWHM) value is about 3.5–4.0°.
- *Focus on sample.* This is a useful configuration if the sample size is small (diameter of the illuminated area on the sample is less than 10 mm under normal incidence), or if particular regions on a sample are

[1] Radiance material types are described in "The Radiance 5.1 Synthetic Imaging System", https://floyd.lbl.gov/radiance/refer/ray.html.

[2] The illuminated area relates to the size of the focus lens. Since the detector distance is about 1000 mm, a larger lens or an off-axis parabolic mirror could extend the diameter to up to 100 mm maintaining far-field conditions.

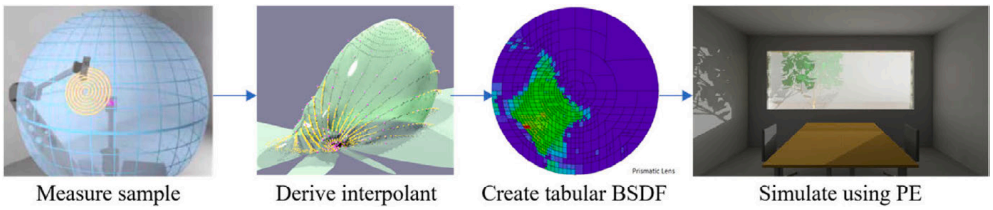

Fig. 1. Workflow for generating and using high-resolution BSDFs.

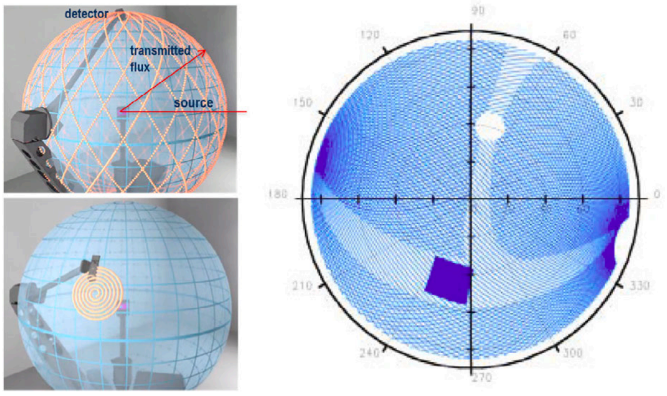

Fig. 2. Path of the full hemispherical scan (upper left), detailed spiral or square scan of a peak region (lower left), and resultant scan pattern (right). Source: Peter Apian-Bennewitz.

to be characterized. FWHM is about 1.5°, about the resolution of the tensor tree with $2^{2\cdot k}$ (k = 7) outgoing directions.

- *Focus on detector.* This is the configuration providing highest directional resolution in near specular measurements. This also implies that the detector-path has to be fine, otherwise one can easily miss peaks in the distribution. The illuminated area on the sample is approximately 20 mm in diameter under normal illumination, so the sample has to be sufficiently large if incident directions close to grazing are to be included. Since the aim is to cover at least four periodical features, this limits the size of structures on the sample to about 5 mm. FWHM is below 1°.

Further increase of the peak resolution is possible only at the expense of a decreased signal if the effective sizes of source and detector were reduced. This would increase the minimum BSDF that can be distinguished from the noise background and thereby affect the accuracy of the measurement of all but the peak directions. The two interdependent properties of near specular resolution and sensitivity (or noise equivalent BSDF) constitute the instrument signature of any goniophotometer. Given its impact on the measured BSDF, a specification of the instrument signature (e.g., a measurement of the unobstructed beam) should be provided with any measured BSDF data.

3.2. Derivation of an interpolant from measured data and generation of the tabulated BSDF

The Radiance tool *pabopto2bsdf* is used to produce scattering interpolants from a sparse set of goniophotometer measurements [37–39]. Additional tools are then used to 1) convert the scattering interpolants into the tabulated BSDF datasets of a specified resolution (*bsdf2klems* and *bsdf2ttree*), and 2) reduce the variable-resolution tensor tree BSDF into a compact data file by merging similar neighboring values (*rttree_reduce*; a "culling" parameter allows the user to reduce the file to a desired size).

For the Klems basis, default parameters were used initially to produce the tabulated BSDF (*-l* 15,000 maximum Gaussian lobes per radial basis function; *-n* 256 samples per patch). These settings were increased (*-l* 0, *-n* 3000; where *-l 0* means that there is no upper limit on the maximum number of lobes) after testing and evaluating noise in the results (Fig. 5).

For the tensor tree basis, interpolation must be done for many incident patches (e.g., 4096 × 4096 incident and exiting directions), taking over an hour for the interpolation, so for each paired direction, a single sample of the interpolant (in the center of the exiting patch) is nominally taken to determine BSDF intensity. After extensive sensitivity testing, modifications were made to the *bsdf2ttree* tool to improve sampling of the peak. If a significant difference in intensity is detected between the target patch and adjacent patches (greater than 35%, where patch order is defined by the Shirley-Chiu representation), then the tool sends 256 sampling rays (with an -n option to override the default) to compute a weighted average BSDF value for the target patch. This improved the estimation of the peak intensity for forward-scattering systems.

Both processes of interpolation and reduction of interpolated data to a discrete angular basis introduce errors between the measured and final tabulated BSDF. A simple example is given to illustrate how the basis resolution modifies the "measured" data. The original analytical BSDF model is shown in blue in the upper left-hand corner and the interpolated representation is shown in the upper right-hand corner of Fig. 6. With the low resolution Klems basis (lower left), transmission values are averaged over a large solid angle. With the high-resolution tensor tree basis (lower right), there is a closer match to the original data set.

3.3. Simulations with peak extraction

3.3.1. Concept

Due to physical limits described in Section 3.1, BSDF measurements have a finite resolution. In the case of pure specular transmission (e.g., clear glass), a goniophotometer with a 0.75° acceptance angle will measure the transmitted light coming out in a cone of about 1.5°. Were we to render the pane of glass based on this measurement, the view outside would be substantially blurred, as would the edges of any sunbeam in the space. If we were to represent the measurements using the Klems BSDF basis, the spread would further increase to about 13°, corresponding to the average resolution of this basis.

These errors are significant for a few reasons. First, any solar patch projected into the room is blurred, distorted, and its intensity is lowered at its edges. Second, narrow, intense light sources such as the sun will be enlarged and dimmed, and therefore misrepresented when directly seen through the BSDF. Third, the view out the glazing system is lost.

One solution to this problem is to include the actual geometry and materials of the shading system in the BSDF file when it is available, as discussed in Section 2.2. For example, Venetian blinds may be represented by the detailed geometry or a BSDF. By switching between representations, global illumination can be computed efficiently, while still having the desired and accurate shadow patterns and striated view out the window. An example is given below. Fig. 7a shows the ground truth for a simple office space with Venetian blinds, rendered using the Radiance *mkillum* program. Fig. 7b shows the same scene rendered using a Klems BSDF representation of the same blinds. Note that the view out the window is blurred, and the sun patch on the wall is similarly spread out. Fig. 7c shows the "proxy" rendering method, where the BSDF for

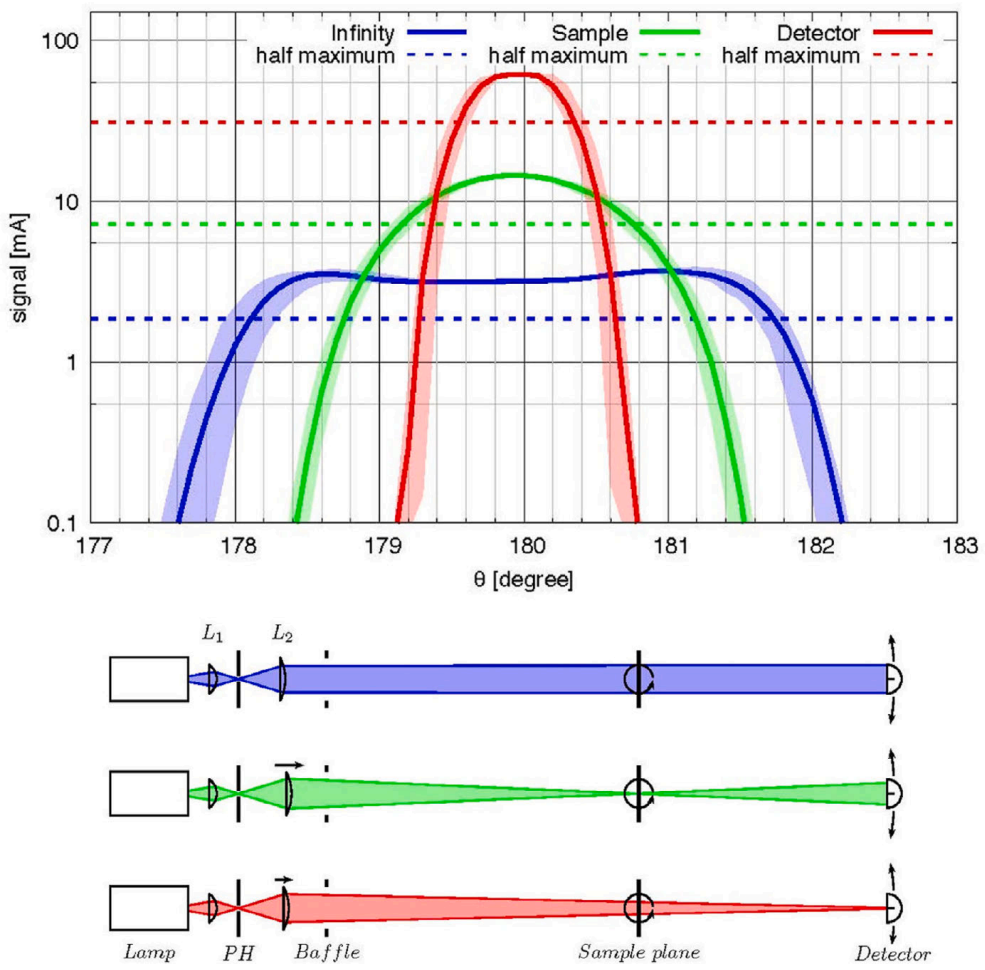

Fig. 3. Beam profiles (above) for three different optical bench configurations (below). Above: The solid profiles are the average over all phi (in-plane) angles. The light shaded areas indicate the variation of the signal depending on phi. Dotted lines show the half maximum, which defines the beam width by its intersection with the solid profiles. Below: The blue configuration (upper) is focused on infinity with FWHM = 3.5°–4.0°. The green configuration (middle) is focused on the sample with FWHM = 1.5°. The red configuration (lower) is focused on the detector with FWHM = 1°. A halogen light source (Lamp), condenser lens (L1), spatial filter (PH), and a focus lens (L2) comprise the illuminator aimed at the sample. Source: HSLU. (For interpretation of the references to color in this figure legend, the reader is referred to the Web version of this article.)

scattered light is combined with the original blinds geometry for seeing and transmitting sunlight through the system. This method is strongly preferred when detailed geometry is available.

When we have BSDF measurements but no system geometry, we need some way to get the rendering closer to ground truth than what is shown in Fig. 7b. Use of a higher-resolution BSDF basis such as the tensor tree results in what is shown in Fig. 7d. Here, there is now a slightly better view out the window and a somewhat cleaner sun patch, but it is still far from matching the ground truth. Moreover, this basis undermines the indirect irradiance caching scheme that accelerates rendering in Radiance due to the smaller scattering profile, forcing use of pure Monte Carlo methods. This takes longer as well as produces noisier results. Therefore, further increasing the directional resolution of BSDF measurements to refine data-driven transmission models is not practical.

If irradiance caching is used, the result is something similar to Fig. 8a, where the calculation is struggling to integrate the solar contribution through the window, leaving splotches from high-variance values in the cache. These errors only get worse as the resolution of the BSDF basis is increased, since this creates even smaller peaks to integrate around the sun.

A "peak extraction" method was developed,[3] which detects when there is a strong peak near the "through" direction in a BSDF, and replaces this peak with a pure specular calculation during shadow testing. The concept behind peak extraction is to allow a finite-resolution representation such as a tensor tree or even Klems basis to have a pure specular ("beam" or "view") component representing a delta function. By specifying an *aBSDF* material, the user is telling Radiance to look for a likely peak in the transmitted direction, and to treat it specially. Rather than light being scattered or spread as would happen normally, rays pass straight through with attenuation corresponding to the BTDF value in that direction. Thus, the sun appears at its original size, objects are visible through the window, beam radiation is permitted, and shadows will be sharp and efficient to compute. The irradiance caching result when applied to the above scene is shown in Fig. 8b. The same "through" component interpretation is used for view and source rays, giving both a clearer view and sharp shadow patterns.

3.3.2. Peak extraction algorithm

Both tensor tree and Klems BSDF bases have a recorded maximum resolution (i.e., smallest represented solid angle). If a peak is found during rendering in the "through" direction whose size corresponds to this maximum resolution, it is extracted and treated as a separate component.

Once a transmitted specular component has been identified, it is assigned an integrated transmission value equal to the BSDF value times the solid angle of the peak patch. The rendering calculation is then altered in the following ways (Fig. 9):

- "Shadow rays" (S) striking the BSDF material will pass directly through, modified by the transmission value in this direction computed from the BSDF, and assigned a solid angle equal to that of the associated source object, which is 0.533° in the case of the solar disc;

[3] Developed by David Geisler-Moroder and Greg Ward, September 2017. Not to be confused with "peak extraction" used in *evalglare*.

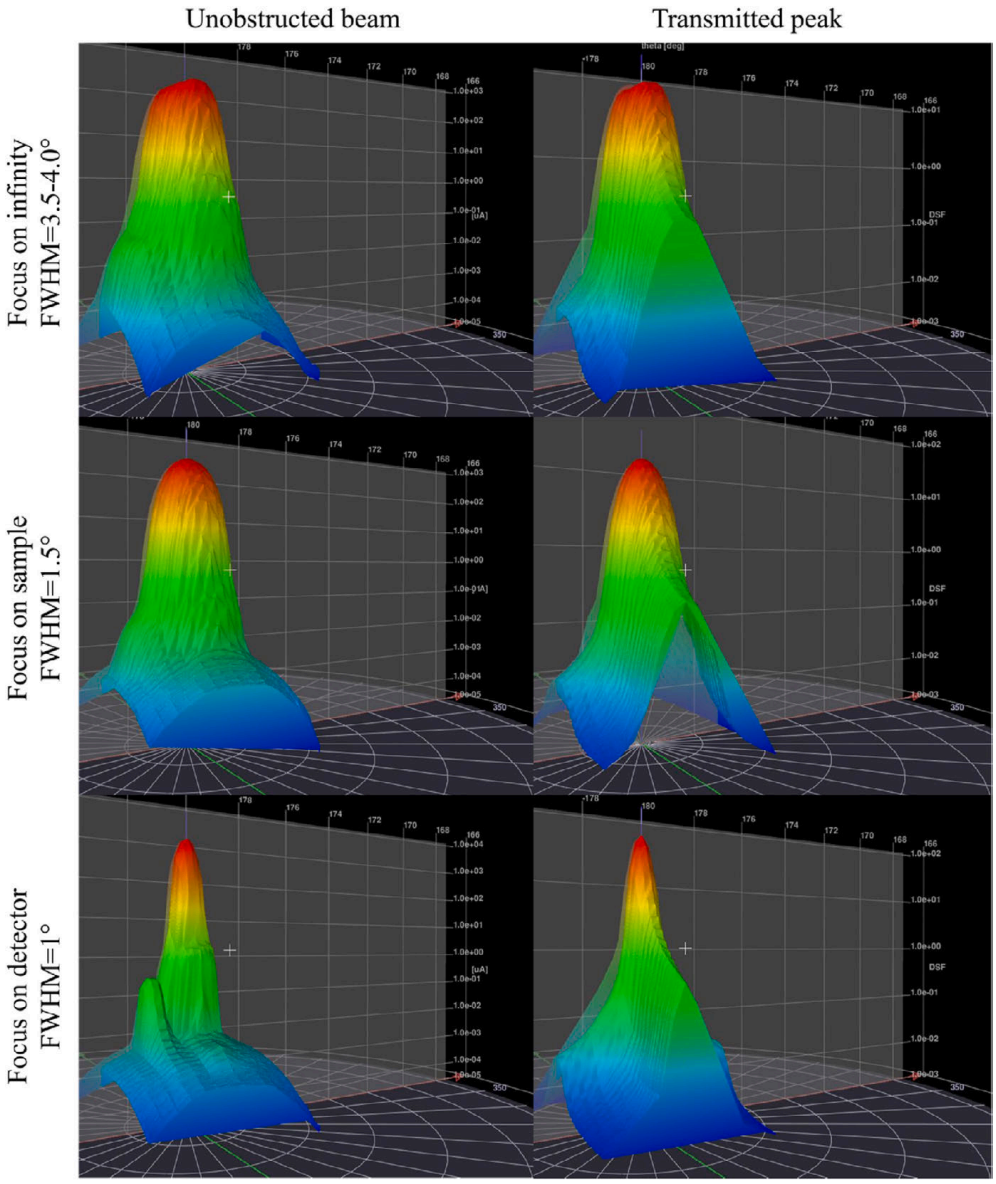

Fig. 4. Intensity distribution of the unobstructed beam (left) and transmitted flux through the roller shade fabric (right), measured at normal incidence. Beam profiles set to focus on infinity, the sample, or the detector. The high resolution achieved by focusing on the detector reveals a weak, secondary artefact caused by the illuminator optics. Source: HSLU. (For interpretation of the references to color in this figure legend, the reader is referred to the Web version of this article.)

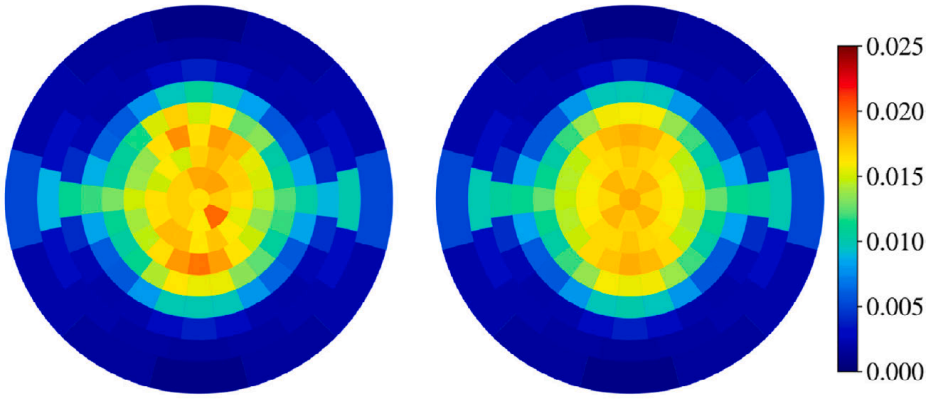

Fig. 5. Direct-hemispherical visible transmittance corresponding to the incident patch direction. Left: transmittance values generated using low sampling settings for *bsdf2klems* (*-l* 15,000, *-n* 256). Right: increased sampling of interpolant (*-l* 0, *-n* 3000). Klems BSDF derived from anisotropic pgII data of the MS6216 fabric. Source: LBNL.

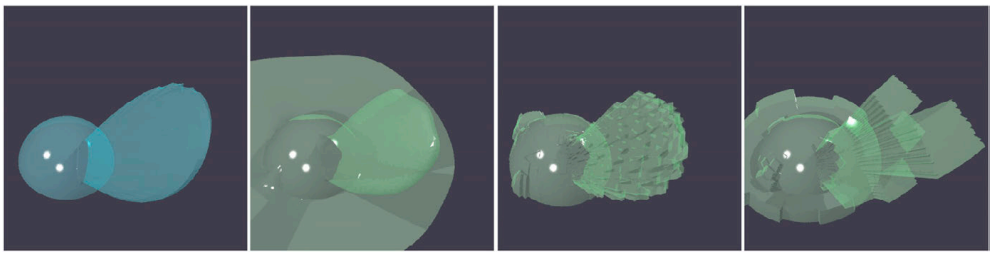

Fig. 6. Synthetic Ward-Geisler-Moroder-Dür BRDF model (left), interpolated distribution (left middle), final distribution with the Klems basis (right middle), and final distribution with the tensor tree representation (right). Source: Anyhere Software.

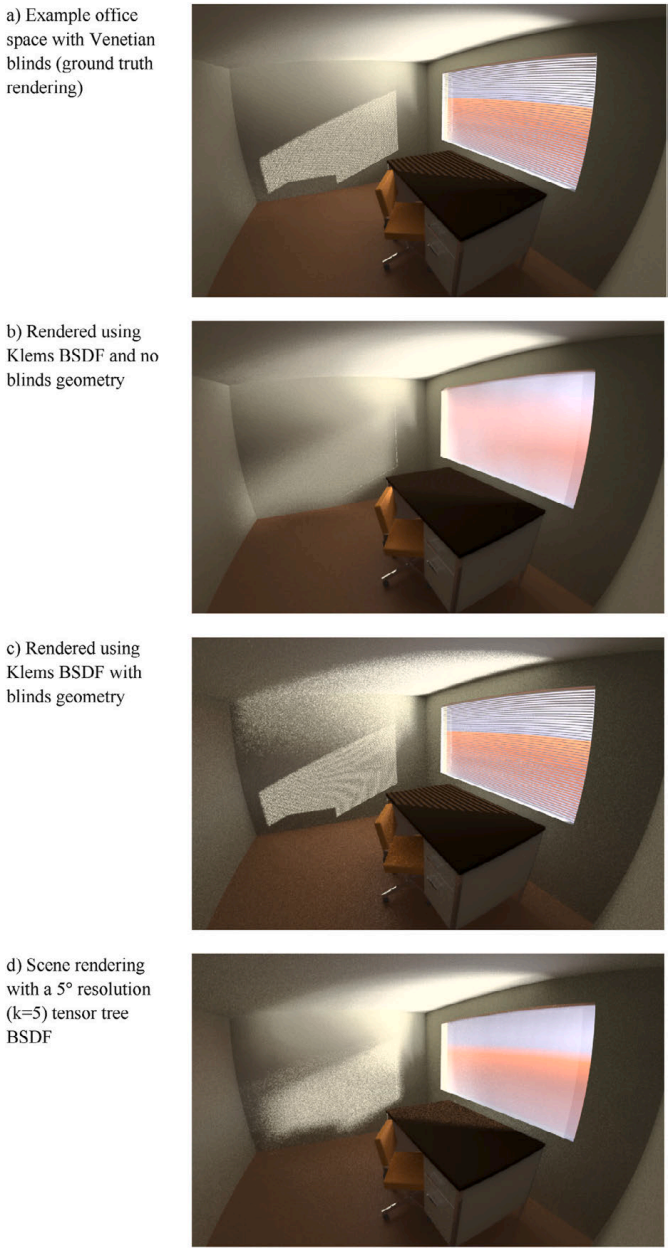

Fig. 7. Renderings of a scene using various methods to represent the Venetian blinds covering the full height of the window. Source: Anyhere Software.

- "View rays" (V) corresponding to line-of-sight are transmitted unperturbed, again modified by the computed transmission value in the respective direction;

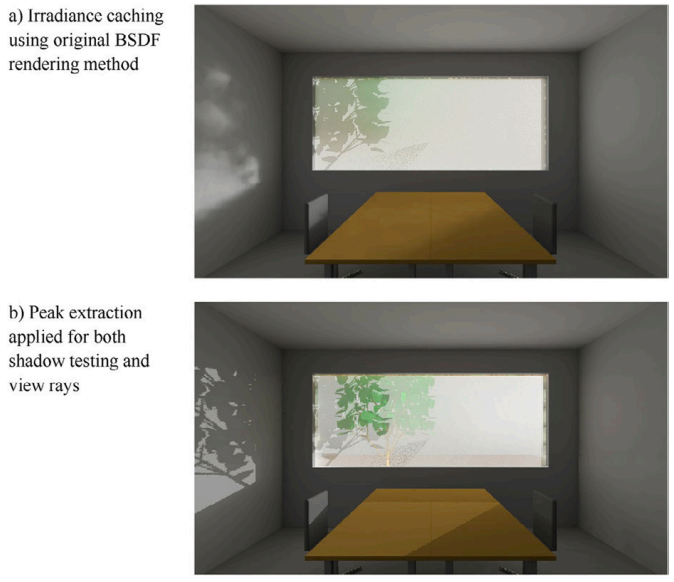

Fig. 8. Renderings of a scene with and without peak extraction to represent specular transmission through a fabric shade with about 2% openness. Source: Bartenbach GmbH. (For interpretation of the references to color in this figure legend, the reader is referred to the Web version of this article.)

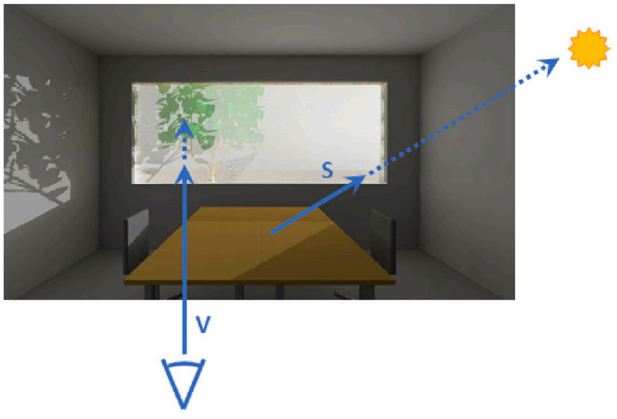

Fig. 9. Example of shadow (S) and view (V) rays (originating from the eye) that benefit from the new peak extraction method. Source: Bartenbach GmbH.

Specular transmission from light sources near the beam direction are attenuated to avoid double-counting contributions. These rays are given an average surrounding brightness ("exclusion zone") determined from 29 peak extraction samples that are not included in the peak value. Also, near-specular transmitted sample rays are rejected to avoid overestimations.

The principal benefit of peak extraction is improved rendering

efficiency and accuracy. By identifying the transmitted peak during BSDF rendering, we can substitute more efficient sampling techniques in both the light source and view ray calculations. This requires only a handful of extra BSDF queries plus some bookkeeping and reduces rendering time substantially by removing a source of severe sampling noise from the calculation.

3.3.3. *Effect of BSDF basis resolution on triggering peak extraction*

Initial testing using peak extraction revealed a codependency of simulated results on BSDF basis resolution. There is an interaction between measurement resolution and BSDF basis resolution that is sometimes problematic. If a tensor tree is used whose maximum resolution is as good or better than the goniophotometer measurements, we may resolve the angular spread of the goniophotometer rather than the system being measured. This may prevent peak extraction from being triggered, since the peak will be spread into a larger region than expected. When the BSDF measurements and basis resolution are similar, we might even extract peaks in some regions and not in others, leading to inconsistent behavior. In such cases, it may be better to lower the tensor tree resolution significantly below that of the goniophotometer when a "through" component is expected, as this will allow peak extraction to work properly. This interplay of different resolutions is a nuisance, as it goes against standard practice and even common sense where one would want to make sure the BSDF basis accuracy is as good or better than the measured data accuracy. At the same time, it is consistent with other optimizations in backward ray tracing. All reflected and scattered components can be efficiently treated by the coarsely resolved BSDF, while the direct component, which is difficult to detect because it comes from a small solid angle (i.e., the solar orb), is treated in a separate way.

3.4. *Modeling point glare sources for use in evalglare*

The *evalglare* tool [40] is used to compute discomfort glare indices such as daylight glare probability (DGP) from simulated or measured high dynamic range (HDR) images. In the original study ([41] with follow-on cross validation work [42]), the DGP metric was derived from human subjects response data correlated to physical measurements of luminance within the field of view; i.e., HDR images taken with a digital camera. Therefore, for simulated renderings generated using peak extraction, the HDR image should be modified to emulate the scatter of light due to the camera lens (i.e., lens flare) prior to analysis with *evalglare*.

In the pilot field study (Section 4), we modified simulated HDR images using a blur filter based on a Lorentzian function with a FWHM of 11.9 arc min (0.18°). The function was derived from optical section retinal images of the eye's vitreoretinal interface from 21 human subjects of varying age between 23 and 70 years old [43]. A function based on the optical performance of the human eye was used assuming that the scatter is approximately the same as that for the HDR camera lens.

The Lorentzian function was implemented as a sum of Gaussian convolutions (blur kernels) on the image via the Radiance *pcomb* tool. The main blur kernel comes in at a little more than 10 cycles per degree, which is the assumed maximum resolution of a standard observer. Two other blur kernels have radii of about 4 and 8 times that, with 11% given to 2.6 cycles/degree and 4% given to 1.4 cycles per degree. This low pass filter only attenuates high frequency signals, as in the narrow luminance peak from the sun in the HDR simulated image. In cases where there is no narrow luminance peak, such as simulated images without peak extraction (Fig. 10d), the blur filter has almost no effect on high intensity regions of the image. Note that this is an approximate implementation

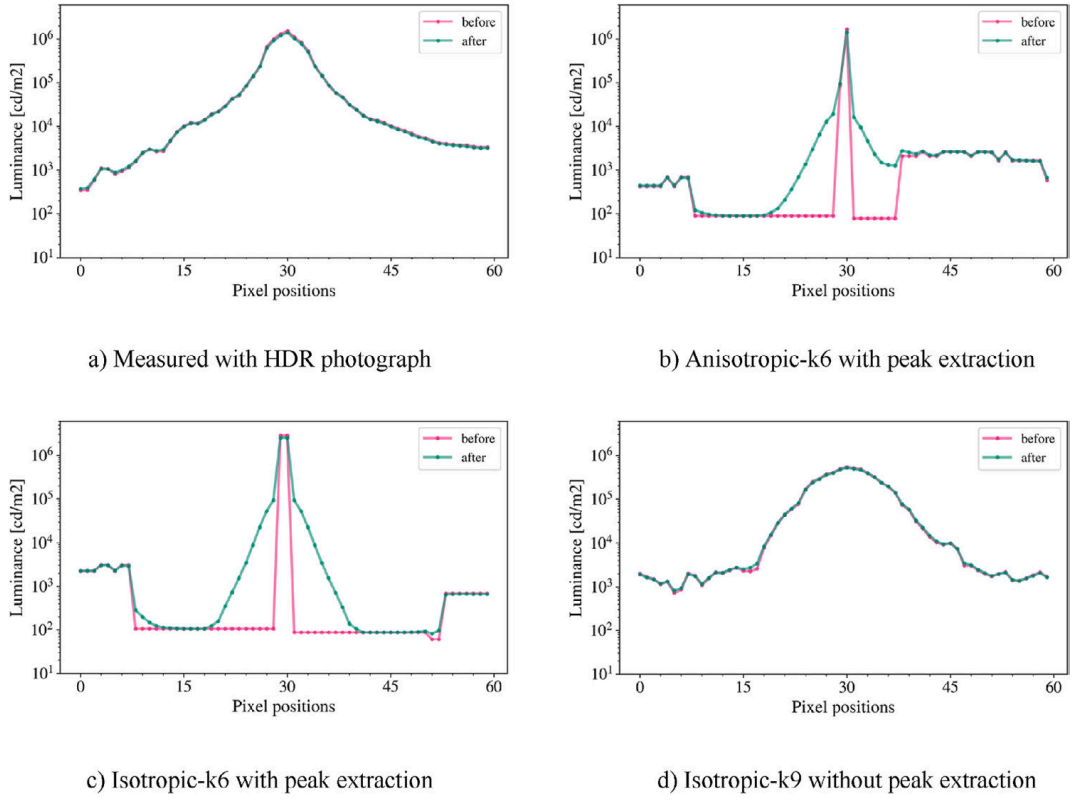

Fig. 10. Luminance (cd/m^2) profile before and after the blur filter was applied. The profile is for a section through the sun and circumsolar region of an HDR image generated by photography in the field (a) or by simulation (b–d) using various high-resolution BSDFs. The pink line is the luminance from the original HDR image. The green line is the luminance after the blur function was applied. If there is a sharp peak in the original distribution (as in the cases with peak extraction (b and c above), the blur function spreads the flux, reduces the peak, and conserves energy. The x-axis is pixel position, where pixel ~30 corresponds to the location of the solar disk and a 60 pixel width represents a 10° subtended angle. The y-axis is pixel luminance (cd/m^2). Label "k6" denotes BSDF resolution of k = 6. Source: LBNL. (For interpretation of the references to color in this figure legend, the reader is referred to the Web version of this article.)

when applied to a fisheye lens since the pixels towards the outer edges are distorted.

An example of a simulated HDR image of a fabric backlit by the sun is given in Fig. 11. For this case, the blur filter spreads the peak luminance from 0.533° to a width of about 1°, with the peak luminance slightly reduced after the blur filter is applied. The HDR image from the outdoor field installation is given in Fig. 12.

4. Pilot validation of BSDF generation methods

The workflow described in Section 3 was applied to a roller shade fabric (MechoShade EuroTwill MS6126-63 black/white, openness factor 1%, visible normal-hemispherical transmittance ($\tau_{nh\text{-}vis}$) 0.03 (manufacturer-provided data), Fig. 13). Fabrics exhibit forward scattering and specular transmission and therefore represent a relevant material type with which to evaluate the workflow. Roller shade fabrics are also used to shade windows in a large fraction of commercial buildings so findings from this study have direct relevance to industry. Comparisons between measured and tabulated BSDF data are given in Section 4.1. Illuminance and luminance measurements taken in a full-scale office testbed were compared to simulated values in Section 4.2.

4.1. Measured and tabulated BSDF data

The BSDF of an A4 size sample of the chosen fabric was measured on HSLU's goniophotometer. To ensure that the illuminated area would not exceed the sample size under oblique illumination, the illuminator was focused on the sample. This achieved a near specular resolution of approximately 1.5° (c.f. Section 3.1). This is wider than the desired 0.5° angular resolution for modeling specular and near specular transmission peaks. Measurements were conducted assuming quadrilateral symmetry; i.e., 45 incident directions for incident angles $\varphi_i = 0°$–$90°$ and $\theta_i = 97.5°$–$180°$ (see Appendix A for Radiance angle convention). Photometric illuminance was recorded by a single Silicon photodiode equipped with a filter to mimic the photopic response of the human eye V(λ). A full spherical scan was conducted first to account for all scattering by reflection and transmission. A second pass was then used to refine peak regions that were found automatically by analysis of the first pass.

The measured pattern of transmission for the MS6216 roller shade fabric sample is shown in Fig. 14 (upper left) for an incident direction of ($\theta_i = 150°$, $\varphi_i = 90°$).[4] The distribution exhibits a distinct peak for specular transmission and a lower intensity star pattern for the scattered transmission surrounding the peak. The measurement requires a high dynamic range to cover the peak values as well as the low diffuse transmission, a sufficient resolution so that no peak values are missed, and is sensitive even to low bias since very low values, which cover large parts of the transmission hemisphere, contribute significantly to total transmission. To test that the measurement, despite these challenges, captures the total transmitted flux, the BSDF was integrated to direct-hemispherical transmission (τ_{dh}) for a set of incident directions. These were compared to the corresponding results of measurements on an integrating sphere by LBNL using a spectrophotometer (Perkin-Elmer Lambda 950, fitted with a 150-mm integrating sphere and a set of angle tubes) using methods defined by Refs. [44,45].[5] Different angle tubes and samples taken from the same fabric swatch were used to measure each angle of incidence.

Direct-hemispherical visible transmittance from integration of the BSDF and integrating sphere measurements are shown in Fig. 15. Integrating sphere data were found to agree with data derived from isotropic goniophotometer measurements to within 0.002 (absolute error) on average over the full range of measured incident angles.

An interpolant was fit to the goniophotometer measurements using the *pabopto2bsdf* tool described in Section 3.2, where the fabric was assumed to be anisotropic (Fig. 14 upper right). Additional examples are given for an alternate interpolation based on a subset of goniophotometer data for ten angles of incidence, assuming the fabric is isotropic (Fig. 14 lower left and right). When these isotropic data sets are used in a rendering, note how the orientation of the potential glare source rotates, depending on which incident phi (φ_i) angle is selected to generate the "isotropic" material (Fig. 16). Note also how the interpolant's peak values for specular transmission are lower than measured values ("$BTDF_{max}$" in Table 2).

To check conservation of energy, direct-hemispherical transmittance and reflectance were computed from the measured BSDF and the tabular models by integration [46] and compared. As shown in Table 2, direct-hemispherical visible transmittance (front, $\theta_i = 30°$) integrals from tabular models were within 0% and 13% of measured values for the isotropic and anisotropic cases, respectively.

To test if the discrepancies between tabulated models and measured BSDF can be explained in part by the underlying assumptions of model generation, direct-hemispherical visible transmittance (front) per incident Klems patch was computed using the anisotropic model, and from isotropic models derived from a subset of goniophotometer data for $\varphi_i = 0°$, 15°, 30°, 45°, and 90°. Comparisons between these plots illustrate that the assumption of isotropic transmission poorly represents the fabric. In the isotropic case for $\varphi_i = 0°$ (Fig. 17 (upper graph, pink line) and Fig. 18), where measurements are biased along the direction of greater scattering (i.e., the ridge in the star pattern in Fig. 14), the interpolant is biased toward higher values near grazing (Klems patch number 70–145), which then spreads this greater scattering around the whole distribution. In contrast, for other phi angles such as $\varphi_i = 30°$ (Fig. 17 lower graph, orange line), the measurements are biased along the direction of less scattering (i.e., the trough of the star pattern), so the interpolant has less scattering and lower values across the whole distribution.

4.2. Field study: illuminance, source luminance, DGP

Simulated data were compared to measured data gathered in a 3.05 m × 4.57 m x 3.35 m (10 ft × 15 ft x 11 ft) south-facing, private office test chamber in the LBNL Advanced Windows Testbed (Berkeley, California; latitude 37.87°N). The MS6216 roller shade fabric was installed (grey side facing indoors) to fully cover the 3.05 m × 2.74 m (10 ft × 9 ft) dual-pane window ($\tau_{vis} = 0.60$) (Fig. 19). Analysis focused on assessing accuracy of glare source luminance, specifically fabric luminance backlit by the sun. Discomfort glare, such as daylight glare probability (DGP), is dependent on accurate modeling of both vertical illuminance (saturation) and luminance of glare sources (contrast) within the field of view. Annualized metrics (e.g., DGP Class) are based on the occurrence and level of discomfort (e.g., intolerable glare for top 5% of the year). For forward scattering materials like fabrics, uncomfortable periods are often defined by direct sunlight transmitted through the shade or areas of the shade backlit by the sun. The annual sunlight exposure (ASE) metric is also sensitive to accurate modeling of the direct sun component [47], but this study omitted further study of modeling horizontal work plane illuminance (evaluated in Ref. [30]).

4.2.1. Field measurements

HDR images were captured every 5 min for a view normal to the window, centered on the width of the window, at a 1.22 m height above

[4] The Mountain software provided by Peter Apian-Bennewitz provides linear interpolation through Delaunay triangulation between scanned points.

[5] The accuracy of the reported values was assessed by repeating the integrating sphere measurement at a 40° angle of incidence ($\varphi_i = 0°$, $\theta_i = 40°$) a total of 16 times. Four separate fabric samples were measured four times each with a small variation in the illuminated area of the sample. This allowed the accuracy to be influenced both by the macroscopic variations in the weave of the material as well as instrument sensitivity to the measured area of the sample. The mean of the 16 measurements was $\tau_{dh\text{-}vis} = 0.0105$ with a standard deviation of 0.0020.

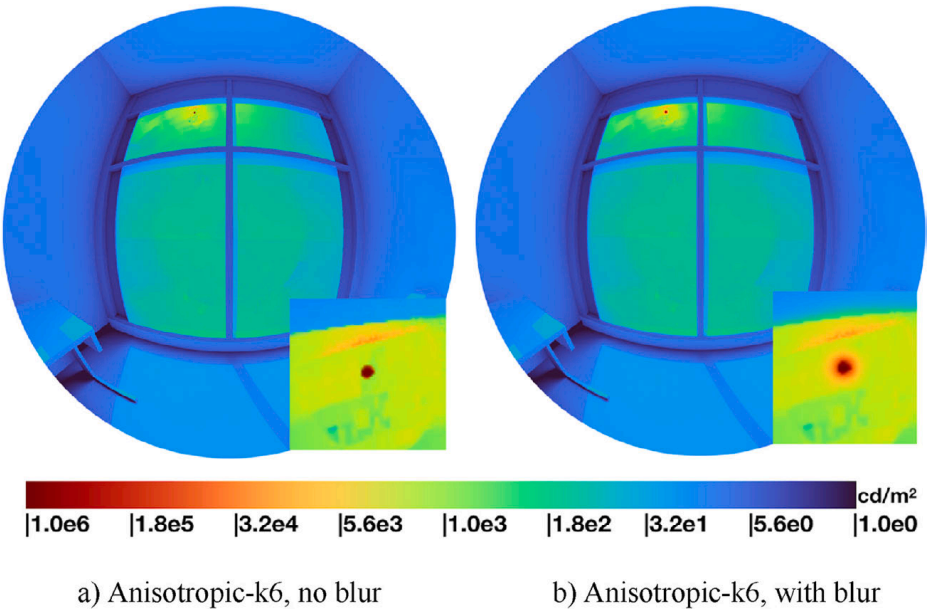

Fig. 11. Simulated HDR image before (left) and after (right) the blur filter was applied. The inset shows an enlarged view of the exclusion zone resulting from triggering of peak extraction (PE) with the sun orb in its center. Source: LBNL.

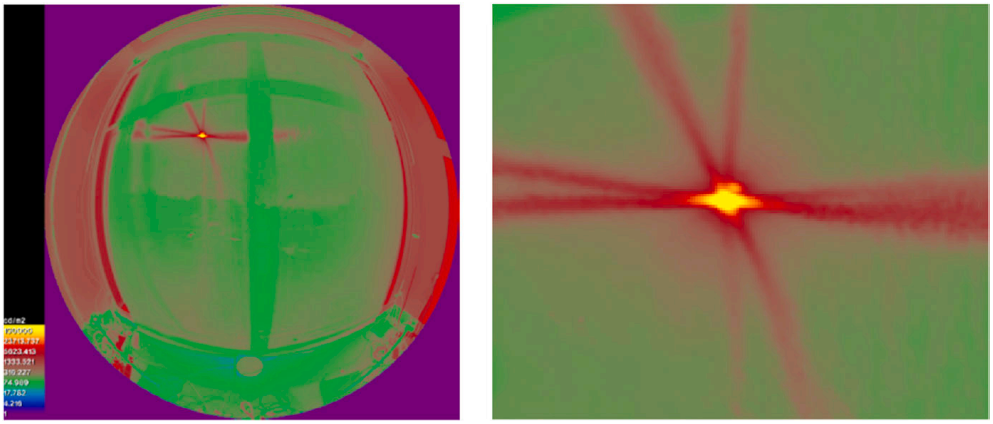

Fig. 12. Measured HDR image (left) and close-up view of the fabric back lit by the sun (right). Source: LBNL.

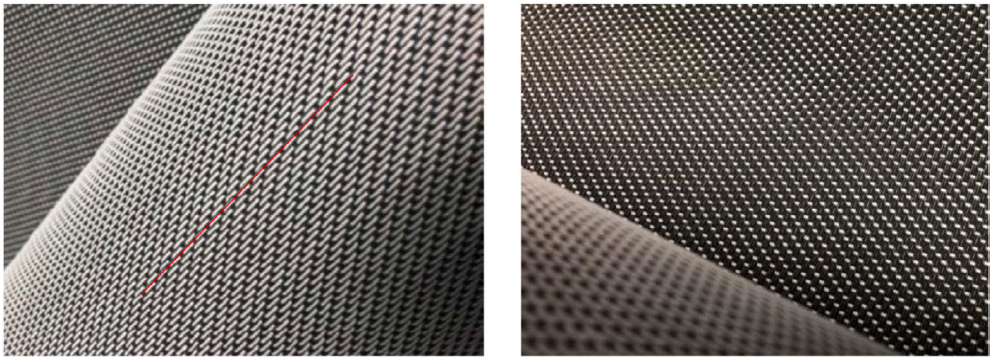

Fig. 13. Photograph of the MS6216 roller shade fabric. The white side faced outdoors (left) and the grey side faced indoors (right). The red line shows the horizontal orientation of the shade installed in the testbed. Source: LBNL. (For interpretation of the references to color in this figure legend, the reader is referred to the Web version of this article.)

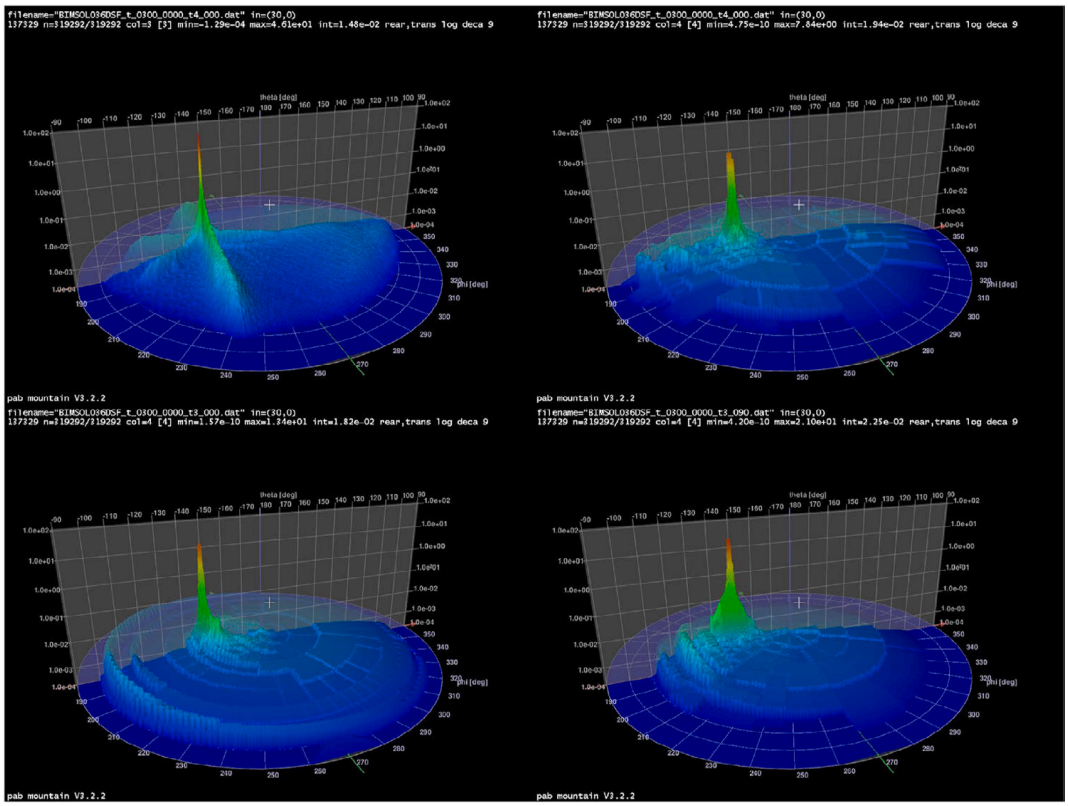

Fig. 14. DSF = BTDF * cos(θ_s) distributions plotted for incident direction $\theta_i = 150°$, $\varphi_i = 90°$ from measurements and the interpolation model, where θ_s is the outgoing scattering θ angle. Distributions are given for the full set of pgII goniophotometer data (upper left), interpolated data derived from the full anisotropic set of goniophotometer data (upper right), interpolated data assuming isotropism for $\varphi_i = 0°$ (lower left), and interpolated data assuming isotropism for $\varphi_i = 90°$ (lower right). MS6216 fabric. Source: HSLU.

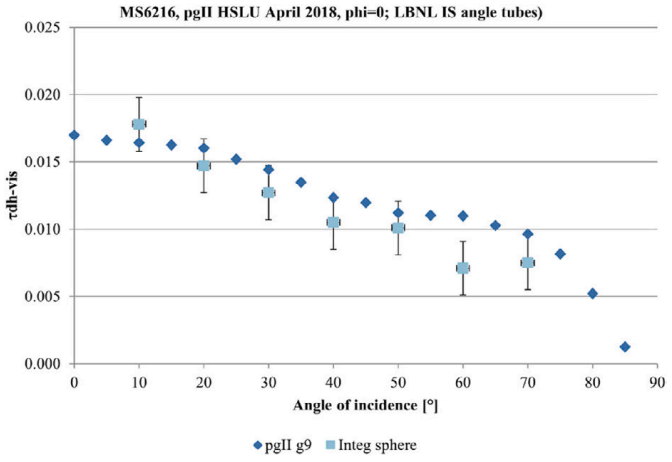

Fig. 15. Direct-hemispherical visible transmittance ($\tau_{dh\text{-}vis}$) as a function of angle incidence for the fabric sample MS6216. $T_{dh\text{-}vis}$ data were derived from interpolated HSLU goniophotometer data (pgII isotropic, $\varphi_i = 0°$, k = 9) or LBNL angle tube integrating sphere measurements. The same standard deviation derived from 16 measurements for $\theta_i = 40°$ is shown with the integrating sphere data for the other angles of incidence ($\theta_i = 10°$–$70°$) in the above plot. Source: LBNL.

the floor, and at a distance of 1.1 m from the window. To measure scene luminance, a series of low dynamic range (LDR) images of varying exposure were taken of the scene using a digital camera (Canon EOS 5D Mark II full frame, Sigma 8 mm f2.8 circular fisheye lens, neutral density filter (ND2), 1200 × 1200 pixels (i.e., approximately 0.20° apex angle minimum)). The LDR images were converted to a high dynamic range (HDR) image using *hdrgen* and the camera's RGB response function. A vignetting correction function, equi-solid-angle to equiangular projection correction function, and a neutral density filter color correction function were applied (equidistant lens for the f5.6 setting). Real-time metered data from a reference luminance meter (Konica Minolta LS-110, 0.33° spot, 0.1 to 999,900 cd/m^2, ±2%) were used to calibrate each HDR image, following methods described in Ref. [48]. The meter was aimed at a backlit square of translucent plastic mounted within a small cutout in the roller shade and located near the center of the HDR image. The metered luminance and HDR-derived luminance for the same area were used to compute a calibration factor which was then applied to the entire HDR image. A cosine-corrected photometric sensor (Li-Cor 210A, ±1% of reading) positioned immediately adjacent to the camera lens was used as a check against HDR-derived vertical illuminance (E_v).

Measurements were conducted from February 22 to March 21 (i.e., $\varphi_i = 38°$–$138°$, $\theta_i = 121°$–$133°$). During this period, HDR-derived vertical illuminance was determined to be in agreement with photometric sensor data within RMSE of ±27.7 lx or 7.74% of measured values (Fig. 20). Data points outside of the 20% deviation range after calibration were excluded from the analysis. For the final analysis, data were selected for sunny periods between 9:00 a.m. and 3:00 p.m. Standard Time when the sun was in the field of view and unobstructed by the window frame or mullions.

Exterior global and direct normal irradiance were measured at a 1-min interval with pyranometer and pyroheliometer sensors (Huseflux SR11 (±1%) and DR01 (±1%), respectively) mounted adjacent to the LBNL testbed. These data were used as inputs to the Perez All-Weather sky luminance model [49] via *gendaylit* [50] to produce the sky matrix used for the Radiance simulations. The sky matrix (**S**) was defined with the Tregenza/Reinhart sky subdivision (MF:4, 2305 patches). The direct

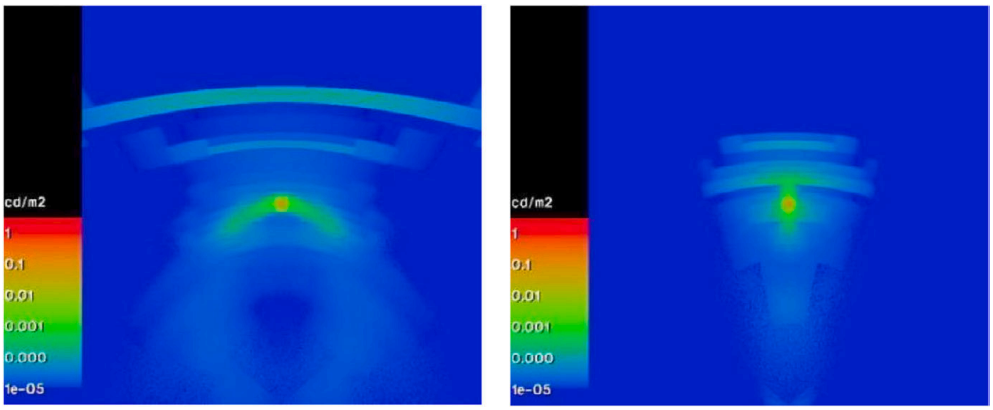

Fig. 16. Renderings of an anisotropic material modeled as an isotropic material. Left: BSDF derived from $\varphi_i = 0°$. Right: BSDF derived from $\varphi_i = 90°$. MS6216 fabric. Source: HSLU.

Table 2
Direct-hemispherical visible transmittance and reflectance derived from tabulated BSDF models versus measured goniophotometer data.

Model	*bsdf2ttree* parameters	Patch apex angle (°)	Incident angle (front) $\theta_i = 30°$, $\varphi_i = 0°$		Inc. angle (back) $\theta_i = 150°$, $\varphi_i = 0°$		$BTDF_{max}$
			$\tau_{dh\text{-}vis}$	$\rho_{dh\text{-}vis}$	$\tau_{dh\text{-}vis}$	$\rho_{dh\text{-}vis}$	
Anisotropic	-t4 g7 t97	1.27	0.017	0.217	0.018	0.407	7.8
Isotropic, $\varphi = 90°$	-t3 g9 t90	0.32	0.015	0.222	0.014	0.415	13.4
Isotropic, $\varphi = 0°$	-t3 g9 t90	0.32	0.017	0.216	0.018	0.402	21.0
Measured, $\varphi = 90°$			0.015	0.241	0.015	0.438	46.1
Measured, $\varphi = 0°$			0.017	0.235	0.018	0.424	–

Notes: τ_{dh}: direct-hemispherical visible transmittance; ρ_{dh}: direct-hemispherical reflectance; front = grey surface of shade facing room, back = white surface facing outdoors (Fig. 13). Isotropic = BSDF derived from $\varphi = 0°$ or $\varphi = 90°$ measured data. *Bsdf2ttree* parameters: rank -t3 isotropic or -t4 anisotropic (automatically determined based on input data); -g *k* = initial tensor tree resolution (see Table 1, $2^{2\cdot k} \times 2^{2\cdot k}$); -t *m* (set to 97 or 90) initial sampling is pared down (culled) by the percentage m. Measured data: pgII goniophotometer with FWHM = 1.5°. Sample orientation (φ, θ) uses Radiance convention where $\varphi = 0°$ is horizontal, $\varphi = 90°$ is up (zenith), and $\theta = 0°$ points inward (indoors). HSLU April 2018 data, MS6216.

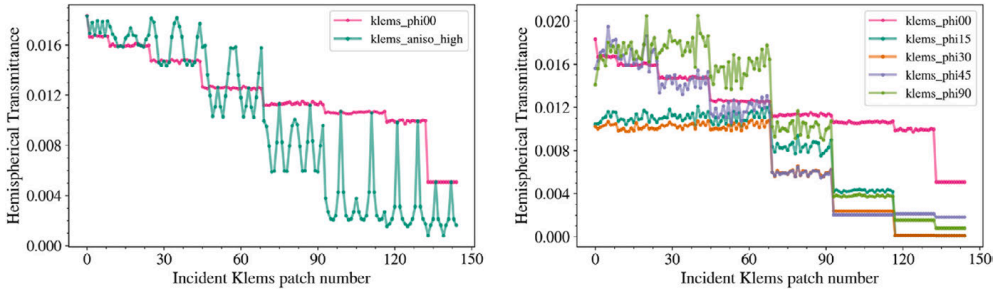

Fig. 17. Direct-hemispherical visible transmittance (front) corresponding to Klems incident patch. Values were derived from the anisotropic interpolant ("klems_aniso_high"), left plot, and isotropic interpolants ("klems_phiN", where N is the φ_i angle), right plot. HSLU April 2018 data, MS6216. Source: LBNL.

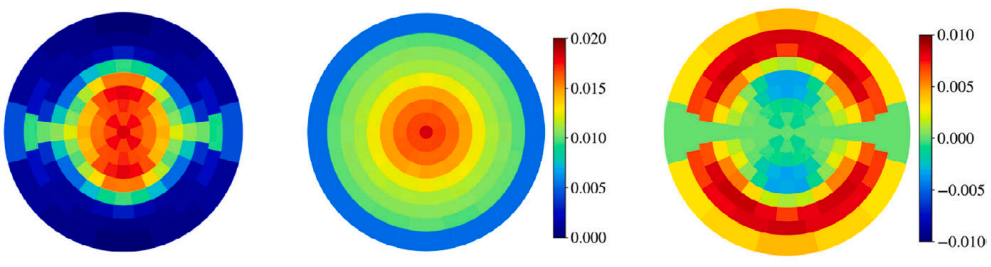

Fig. 18. Direct-hemispherical transmission per Klems patch incident direction generated using the a) anisotropic and b) isotropic $\varphi_i = 0°$ interpolant; c) is the absolute difference in BTDF coefficients between the two cases. Values for the isotropic case are significantly overestimated within the $\theta = 50°$–$90°$ range. System values (glass + MS6216 shade) produced by *genBSDF*. Source: LBNL. (For interpretation of the references to color in this figure legend, the reader is referred to the Web version of this article.)

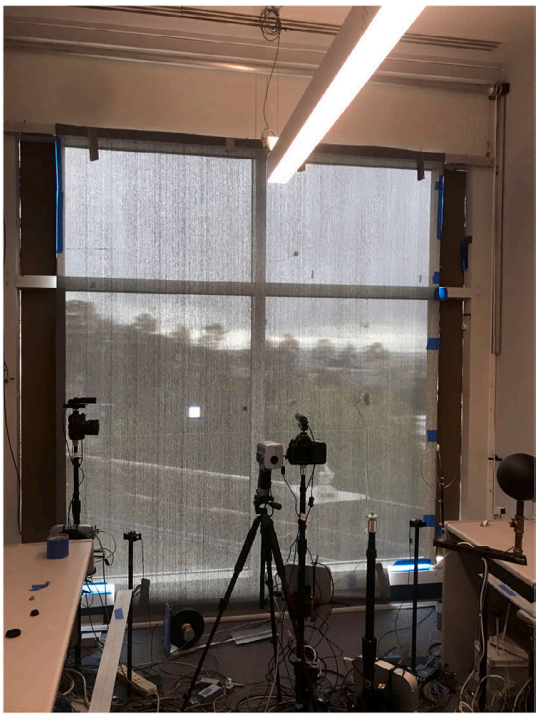

Fig. 19. Indoor view of the LBNL testbed office looking toward the south-facing window with the MS6216 roller shade fabric. The small square cut out is located in the lower left window at seated eye height. The gaps between the face of the window glass and the shade were blocked off on each side of the shade to simplify the simulation model. Unshaded portions of the window on the side were also blocked off. The electric lights (shown as "on" in this photograph) were turned off. Source: LBNL. (For interpretation of the references to color in this figure legend, the reader is referred to the Web version of this article.)

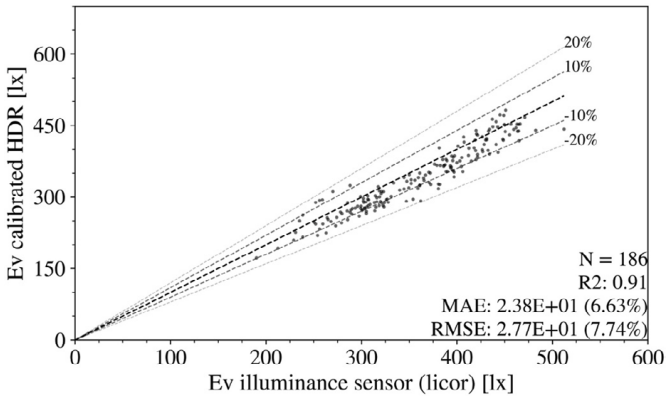

Fig. 20. Comparison between vertical illuminance measured by the photometric sensor located next to the HDR camera's lens and vertical illuminance (lx) calculated from the camera's HDR image for all monitored days. Points outside of the 20% deviation range after calibration were excluded from the analysis. Source: LBNL.

sun matrix ($\mathbf{S}_{sun}$) was derived from direct normal irradiance measurements, which included the circumsolar region (approximately 6° apex angle). *Gendaylit* (by default) uses a Perez-derived function to model the exponential falloff in luminance between the sun and circumsolar region.

4.2.2. Simulation method

Tabulated BSDFs were generated from HSLU goniophotometer measurements of the MS6216 shade fabric. Interpolants were derived from the anisotropic and isotropic ($\varphi_i = 0°$) datasets using the methods described in Section 3.2. Each interpolant was then used to produce the tabulated BSDF for the Klems (*bsdf2klems*) and tensor (*bsdf2ttree*) bases. 80% of the tensor elements were culled in the data-reduction pass.

The shade layer BSDFs (denoted with the "-s" suffix) were produced as follows:

Case	Description
Isotropic-k6-s	Isotropic interpolant based on $\phi_i = 0°$ data, tensor tree model, $k = 6$ (*bsdf2ttree* -g 6 -t 80)
Anisotropic-k6-s	Anisotropic interpolant assuming quadrilateral asymmetry, tensor tree model, $k = 6$ (*bsdf2ttree* -g 6 -t 80)
Anisotropic-k5-s	Anisotropic interpolant assuming quadrilateral asymmetry, tensor tree model, $k = 5$ (*bsdf2ttree* -g 5 -t 80)
Anisotropic-Klems-s	Anisotropic interpolant assuming quadrilateral asymmetry, Klems basis (*bsdf2klems*)

The modeled fenestration system consisted of several layers: 1) a double-pane clear glazing unit ($\tau_{vis} = 0.60$), modeled as a Radiance *BRTDFunc* material type [51], and 2) the MS6216 shade fabric installed on the indoor side of the glazing unit. The tabulated BSDFs were combined using *genBSDF* to produce the final system BSDF as follows:

BSDF case	Glass layer	Shade layer	*genBSDF* options
Isotropic-k6	BRTDFunc	Isotropic-k6-s	-t3 6
Anisotropic-k6	BRTDFunc	Anisotropic-k6-s	-t4 6
Anisotropic-k5	BRTDFunc	Anisotropic-k5-s	-t4 5
Anisotropic-Klems	BRTDFunc	Anisotropic-Klems-s	

The ray-tracing simulations (*rtrace*) were performed using the 1-min monitored solar irradiance data as input with parameter settings aimed towards accuracy rather than that of a typical end user: i.e., *ab 6 ad 262144 lw 1e-9*. The *BSDF* material type was used to model cases with no peak extraction. The *aBSDF* material type was used to model cases with PE.

4.2.3. Results: vertical illuminance

To assess conservation of energy within the field of view, vertical illuminance (E_v) was simulated at the photometric sensor location using BSDFs of various resolutions with and without the use of the peak extraction (PE) algorithm. Measured photometric sensor data were in the range of 200 lx–500 lx, due to the low-transmission properties of the fabric. Use of the PE algorithm reduced error compared to simulations without PE. With isotropic-k6 BSDF data and PE, simulations resulted in a significant overestimation of E_v due to overestimation of direct-hemispherical transmission $\tau_{dh,vis}$ at the more oblique incident angles (RMSE = 118 lx, see Section 4.1). With anisotropic BSDF data and PE, simulation errors were lower (RMSE = 50 lx–90 lx).

The fabric was assumed to have quadrilateral symmetry so goniophotometer measurements were made for the $\varphi_i = 0°$–90° quadrant. Simulation errors were lower for angles of incidence corresponding to $\varphi_i < 90°$ (RMSE = 32 lx–63 lx, see Fig. 21) and greater for $\varphi_i > 90°$, indicating that the fabric in fact exhibited asymmetric scattering behaviour over the vertical plane.[6] For the subset of periods when sunlight was transmitted specularly through the fabric, triggering PE, errors were also lower: RMSE = 32 lx–43 lx, 9.6%–12.2% (Fig. 22). Errors are summarized in Table 4 and Fig. 29 at the end of Section 4.

4.2.4. Results: source luminance

To assess conservation of energy within a specified cone of view, measured and simulated average luminance for a 2° (sun and circumsolar region plus human blur) and 3° cone centered on the sun disc were

[6] This interpretation was confirmed by additional measurements with incident $\varphi_i = 0°$–360°.

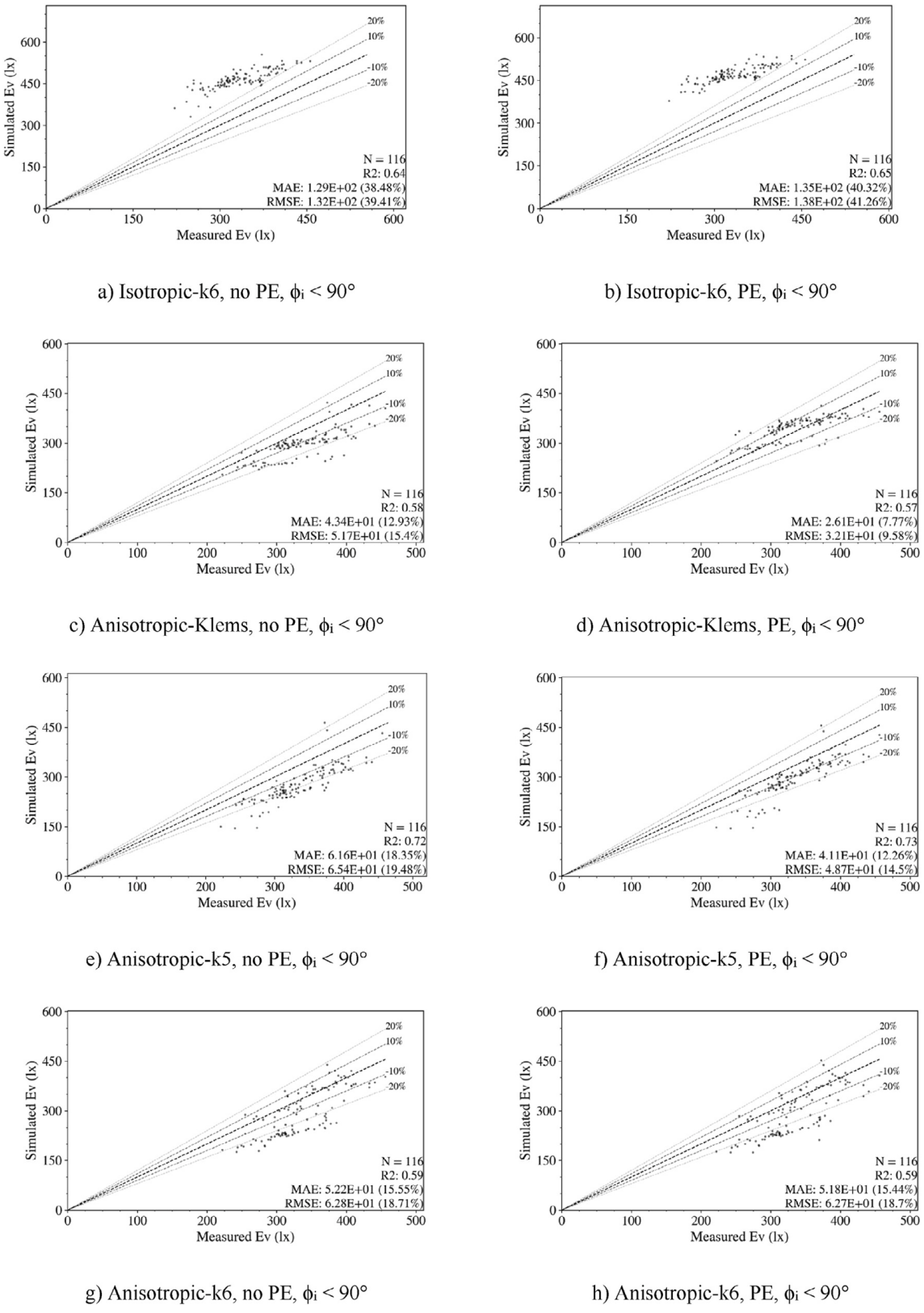

Fig. 21. Measured vertical illuminance (x-axis, E_v (lx)) versus ray-tracing simulations of vertical illuminance (y-axis) for $\varphi_i < 90^\circ$ incident angles. The no-PE and PE cases were modeled with the *BSDF* and *aBSDF* material, respectively. Source: LBNL.

compared on clear sunny days. Analysis was restricted to times when PE was triggered and when the sun's angle of incidence was within $\varphi_i < 90^\circ$. This assessment provides insights as to whether forward scattered energy from the sun is being distributed to the proper regions within the scene.

Luminance data were extracted from HDR simulated and measured images. The location of the sun was first identified by pixels with the highest scene luminance then secondary checks were performed to

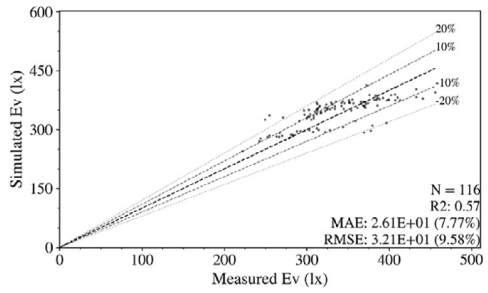

a) Anisotropic-Klems, PE triggered, $\phi_i < 90°$

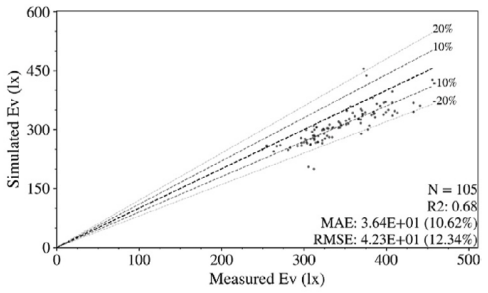

b) Anisotropic-k5, PE triggered, $\phi_i < 90°$

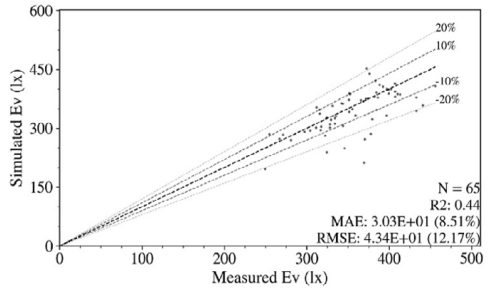

c) Anisotropic-k6, PE triggered, $\phi_i < 90°$

Fig. 22. Measured vertical illuminance (x-axis, Ev (lx)) versus simulated values (y-axis) for angles of incidence when $\varphi_i < 90°$ and when PE was triggered. Source: LBNL.

Table 3
Evalglare analysis of simulated HDR images (shown in Fig. 25) and respective measured HDRs.

	Ls (cd/m^2)	Omega (sr)	Apex angle (°)	DGP	E_v (lx)
evalglare: simulated images					
Fig. 25a	1,194,344	0.000104	0.66	0.350	293.9
Fig. 25b	592,701	0.000061	0.50	0.250	229.1
Fig. 25c	8961	0.004908	4.53	0.138	206.5
Fig. 25d	11,534	0.006747	5.31	0.142	200.5
evalglare: measured images					
Fig. 25a	291,038	0.000429	1.34	0.293	335.42
Fig. 25b	431,956	0.000476	1.41	0.323	377.09
Fig. 25c	149,534	0.000306	1.13	0.232	258.35
Fig. 25d	255,149	0.000399	1.29	0.277	283.94

ensure that the x-y coordinates were in agreement with calculated locations of the sun orb. Datapoints were filtered to exclude times when the sun was obstructed by window mullions. All sun positions within the field of view were included despite some inclusion of opaque elements within the cone of view. The luminance of the sun is orders of magnitude greater than opaque elements, so inclusion of frame elements is unlikely to affect the comparisons. The blur filter described in Section 3.4 was applied to all simulated HDR images.

Measured and simulated source luminance are shown in Fig. 23. For the 3° cone, the simulated case using isotropic BSDF data performed poorly (RMSE = 87,900 cd/m^2) compared to anisotropic cases (RMSE = 15,700 to 34,800 cd/m^2) for the same reason stated for vertical illuminance. Measured luminance ranged from 27,000 to 123,000 cd/m^2. The anisotropic-k5 case performed better than the anisotropic-k6 case while the anisotropic-Klems case performed worse, illustrating the co-dependency between triggering of PE and BSDF basis resolution discussed in Section 3.3.3. Similar trends were observed for the 2° cone source luminance. Measured luminance values also varied significantly over short periods on stable, clear sunny days, indicating that fabric variations were another source of error.

If one parses the data by bins of incident angle, we can attribute some of the larger errors to periods when the angles of incidence were more oblique. For the anisotropic-k5 case, peak extraction was triggered within a range of $\varphi_i = 40°–90°$ and $\theta_i = 125°–140°$ (Fig. 24). Errors tended to be greater for $\varphi_i < 70°$.

This behavior can be explained in the following example. As the sun transitions to oblique angles of incidence, peak extraction (PE) transitions from full to partial PE triggering (with local noise) to no PE at all, resulting in poorer model performance.

- In the through direction, PE is triggered and the sun source is modified by specular transmission estimated from the near-peak values of BSDF (dark red point in the center of the exclusion zone, Fig. 25a).
- As the sun moves to a more oblique angle (Fig. 25b and c), "partial" PE triggering occurs, where PE may or may not occur for the sun source (notice dark red point and exclusion zone occurs in Fig. 25b but not in Fig. 25c). Additional bright pixels appear within the exclusion zone due to non-PE throughput from the sun in the near-peak direction of the BTDF. The discrete boundaries of the checkerboard pattern within the exclusion zone are edges corresponding to the tensor tree patch directions.
- When PE is not triggered (Fig. 25d), there is no exclusion zone and flux in the through direction is assigned an intensity based on the tensor tree resolution.

Errors are summarized in Table 4 and Fig. 29 below.

4.2.5. Results: daylight glare probability (DGP)

We used *evalglare* (version 2.07) to extract glare source and vertical illuminance data from simulated and measured HDR images, then compute daylight glare probability (DGP). *Evalglare* employs various methods to identify whether a pixel qualifies as a glare source and then aggregates adjacent qualifying pixels within a specified search radius. We used the threshold method which identifies all pixels greater than a specified threshold (i.e., 2000 cd/m^2) as a glare source. Pixels with a

Table 4
R-squared for linear regression model, RMSE, and MAE between measured and simulated E_v (lx), source luminance for 3° cone (cd/m^2) and DGP for various modeled cases.

E_v (lx)		No PE		PE		PE, $\varphi_i < 90°$		PE-trig, $\varphi_i < 90°$	
Isotropic-k6	R^2	0.25		0.32		0.65		0.65	
	RMSE	112.0	−30.74%	118	−32.39%	138.0	−41.26%	138.0	−41.26%
	MAE	99.6	−27.33%	106	−29.03%	135.0	−40.32%	135.0	−40.32%
Anisotropic-Klems	R^2	0.41		0.50		0.57		0.57	
	RMSE	84.4	−23.18%	50.2	−13.78%	32.1	−9.58%	32.1	−9.58%
	MAE	69.9	−19.19%	39.8	−10.92%	26.1	−7.77%	26.1	−7.77%
Anisotropic-k5	R^2	0.45		0.50		0.73		0.68	
	RMSE	91.9	−26.03%	78.7	−21.60%	48.7	−14.50%	42.3	−12.34%
	MAE	78.6	−22.25%	65.7	−18.04%	41.1	−12.26%	36.4	−10.62%
Anisotropic-k6	R^2	0.38		0.39		0.59		0.44	
	RMSE	91.8	−25.21%	90.4	−24.81%	62.7	−18.70%	43.4	−12.17%
	MAE	77.0	−21.14%	75.6	−20.75%	51.8	−15.44%	30.3	−8.51%

Ls-3° (cd/m^2)		PE, $\varphi_i < 90°$		PE-trig, $\varphi_i < 90°$	
Isotropic-k6	R^2	0.23		0.23	
	RMSE	87,900	−130.29%	87,900	−130.29%
	MAE	85,700	−127.10%	85,700	−127.10%
Anisotropic-Klems	R^2	0.19		0.19	
	RMSE	32,100	−47.60%	32,100	−47.60%
	MAE	28,000	−41.47%	28,000	−41.47%
Anisotropic-k5	R^2	0.49		0.44	
	RMSE	18,900	−28.07%	15,700	−22.36%
	MAE	14,300	−21.24%	12,100	−17.24%
Anisotropic-k6	R^2	0.43		0.19	
	RMSE	34,800	−51.61%	23,200	−29.46%
	MAE	29,000	−43.06%	18,000	−22.88%

DGP		PE, $\varphi_i < 90°$		PE-trig, $\varphi_i < 90°$	
Isotropic-k6	R^2	0.26		0.26	
	RMSE	0.077	28.74%	0.077	28.74%
	MAE	0.073	27.12%	0.073	27.12%
Anisotropic-Klems	R^2	0.52		0.52	
	RMSE	0.058	21.73%	0.058	21.73%
	MAE	0.055	20.50%	0.055	20.50%
Anisotropic-k5	R^2	0.30		0.58	
	RMSE	0.058	21.79%	0.037	13.48%
	MAE	0.044	16.46%	0.033	12.27%
Anisotropic-k6	R^2	0.42		0.28	
	RMSE	0.079	29.63%	0.040	14.14%
	MAE	0.068	25.43%	0.036	12.76%

luminance greater than 50,000 cd/m^2 were extracted as separate glare sources.[7] The search radius was set to 0.2 radians (11.5°).

Comparisons between measured and simulated DGP revealed that when specular transmission occurred (worst case glare condition), simulated results overestimated DGP by a minimum RMSE of 0.037 (13.48%) for the best case (anisotropic-k5 BSDF, Fig. 26). An absolute DGP difference of 0.04 defines the difference between discomfort glare levels, so this error is significant.

Fig. 27a illustrates the size and shape of the solar peak identified using the *evalglare* peak threshold of 50,000 cd/m^2. The measured HDR image (red) indicates additional forward scattering in the horizontal direction, whereas the simulated, peak-extracted, solar peak (blue) remains circular. Fig. 27b and c shows the peak shape when we take a cross-section in the horizontal and vertical direction. The measured peak is spread wider in the horizontal direction (also shown in Fig. 27a: red), and narrower in the vertical direction. The blurring algorithm that is applied on the peak-extraction solar peak reduces the solar intensity and increases the solid angle so that it matches well to the measured shape in the vertical direction. Areas under the curves and above the red dotted line (50,000 cd/m^2) indicate the two-dimensional energy detected by *evalglare* for the peak glare source. Differences in energy in these areas are the main cause of differences in DGP between measured and simulated results.

For oblique angles of incidence when the sun source is partially or just fully obscured by the fabric (Fig. 25c and d) and PE is not triggered, the reverse is true: DGP is underestimated. For this example, the simulated glare source is 16 times less intense and 16 times larger than the glare source identified in the measured HDR image (Table 3). In the case of the simulated images, noisy pixels from stochastic Monte Carlo sampling within and slightly outside of the exclusion zone affects *evalglare's* identification, intensity, and solid angle of the glare sources.

Fig. 28 shows the solar luminance for varying solid angles centered around the solar disk. The difference between the measured and simulated source luminance differs the most when evaluating a cone with a 0.533° subtended angle. This difference decreases as the subtended angle is increased to 3° around the solar centroid, illustrating that forward scattering energy is conserved but is distributed differently between simulated and measured results. So while source luminance was found to be adequately simulated for the same cone of view (i.e., 2° and 3°), the solid angle and luminance of the solar glare source detected by *evalglare* were not the same between simulated and measured HDR images.

5. Discussion

In the field study, potential sources of error include variations in the weave of the fabric, differences in weave between the sample measured in the goniophotometer and that used in the field test, and variations in

[7] This is the default "peak extraction" feature of *evalglare*, which is not to be confused with the BSDF peak extraction model described in Section 3.3.

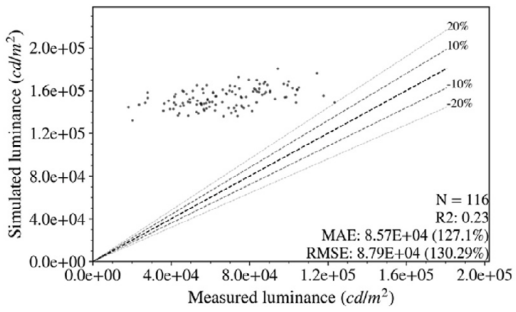

a) Isotropic-k6, PE triggered, 3°, $\phi_i < 90°$

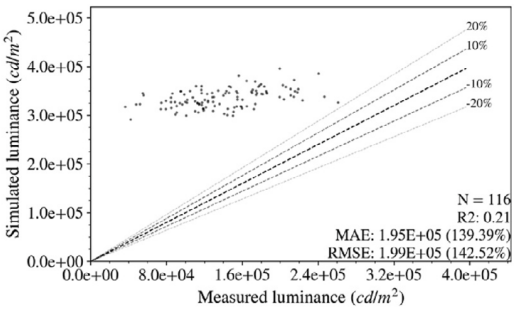

b) Isotropic-k6, PE triggered, 2°, $\phi_i < 90°$

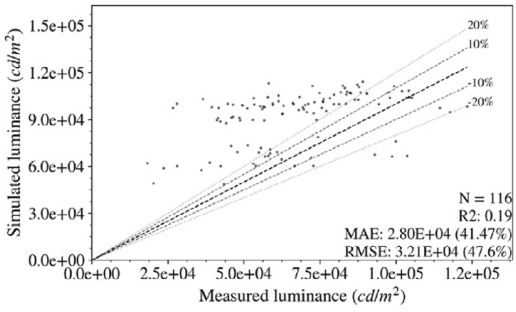

c) Anisotropic-Klems, PE triggered, 3°, $\phi_i < 90°$

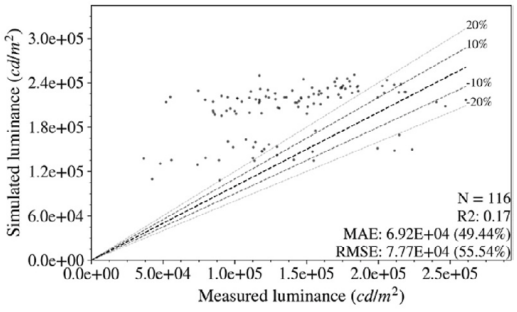

d) Anisotropic-Klems, PE triggered, 2°, $\phi_i < 90°$

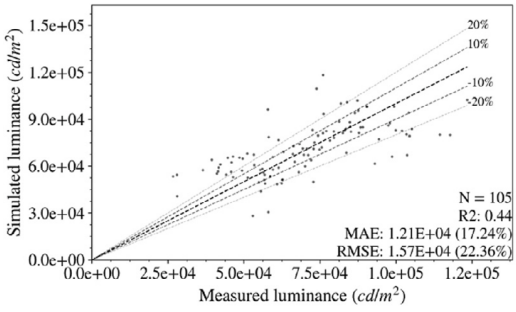

e) Anisotropic-k5, PE triggered, 3°, $\phi_i < 90°$

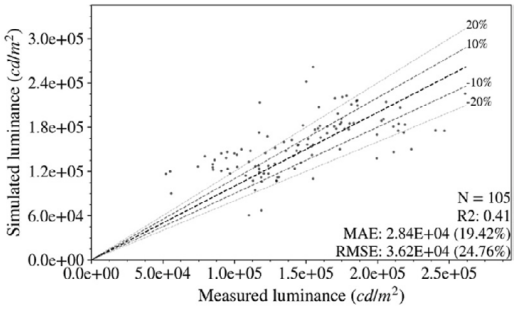

f) Anisotropic-k5, PE triggered, 2°, $\phi_i < 90°$

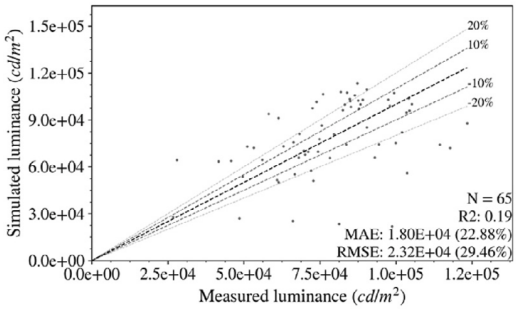

g) Anisotropic-k6, PE triggered, 3°, $\phi_i < 90°$

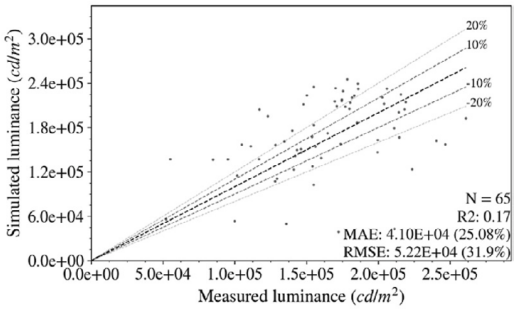

h) Anisotropic-k6, PE triggered, 2°, $\phi_i < 90°$

Fig. 23. Measured (x-axis) versus simulated (y-axis) luminance of the sun and surrounding area for subtended angles of 3° (left) and 2° (right). Clear sunny days only. Anisotropic and isotropic BSDF data, triggered PE, $\varphi_i < 90°$, with blur filter. Source: LBNL.

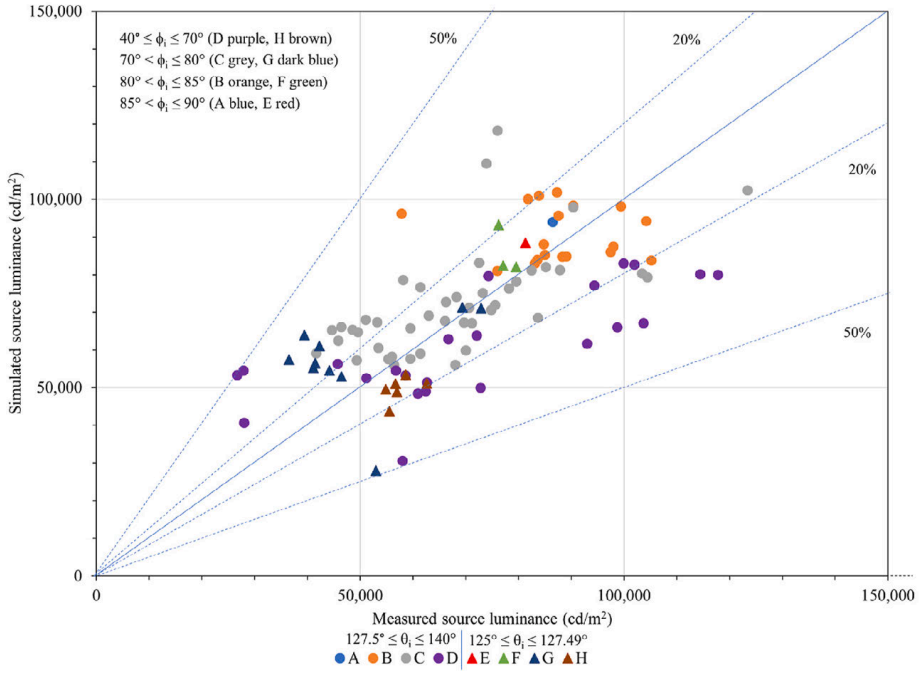

Fig. 24. Anisotropic-k5 case (RMSE = 15,700 cd/m^2 (22.36%), $r^2 = 0.44$). Measured versus simulated luminance of the sun for subtended angle of 3° on clear sunny days, PE triggered, blur filter. Points A-D are for 127.5° < θ_i < 140°. Points E-H are for 127.49° < θ_i < 125°. Points A-D are and E-H are distinguished by the ranges φ_i = 40°–70°, 70°–80°, 80°–85°, and 85°–90°. Source: LBNL.

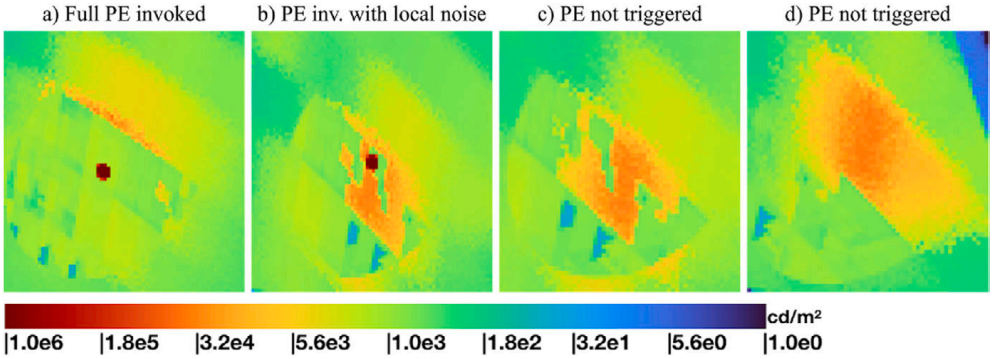

Fig. 25. Example simulated HDR images with peak extraction at various stages of being triggered. Anisotropic-k6, February 22, 14:00 to 14:30 ST. Source: LBNL.

the drape of the fabric from the ideal plane represented by the simulations. Field-related errors could have originated from positional differences between the measured and simulated sensor points and errors in monitored HDR luminance (e.g., properties of the neutral density filter and reference diffusing film, etc.). Exterior global and direct normal irradiance were used as inputs to the Perez All-Weather sky luminance model. This includes two potential sources of error: first, the spatial distribution of the sky luminance and second, the luminous efficacy estimation to convert radiometric to photometric units. Both vary from the real-world situation. While the former is of less importance as long as the proportion between sky and sun are assigned correctly, the latter influences the overall luminous flux impinging at the façade. Photometric instead of radiometric measurements can solve the latter; using calibrated HDR environment maps can solve both.

5.1. Assessment of errors across the workflow

Barring these field-related errors, summary findings derived from the pilot validation study are as follows:

- Comparisons between tabular BSDF data and two independent sources of data (i.e., integrated sphere measurements and data derived directly from measured goniophotometer data, cf. Section 4.1) demonstrated that there were small absolute differences in direct-hemispherical transmittance and reflectance when the tabular BSDF data were derived from adequate goniophotometer measurements. If the material is assumed to be isotropic when it is in fact anisotropic, the resultant tabular BSDF data can deviate in some regions. If the material is assumed to be quadrilaterally symmetric when it is in fact bilaterally symmetric, similar errors are incurred. For this study, assumptions of isotropic properties resulted in significant errors in predicted vertical illuminance and source luminance (Section 4.2). Assumptions of quadrilateral symmetry were better but still showed some bias.
- For sunny periods when specular transmission occurred, simulations with peak extraction yielded good agreement with measured source luminance data (i.e., 2° and 3° cones centered on the solar disc, cf. Section 4.2.4). Anisotropic BSDFs outperformed isotropic BSDFs. However, increasing resolution of the anisotropic tensor tree BSDFs beyond some point did not further improve accuracy (cf. Section

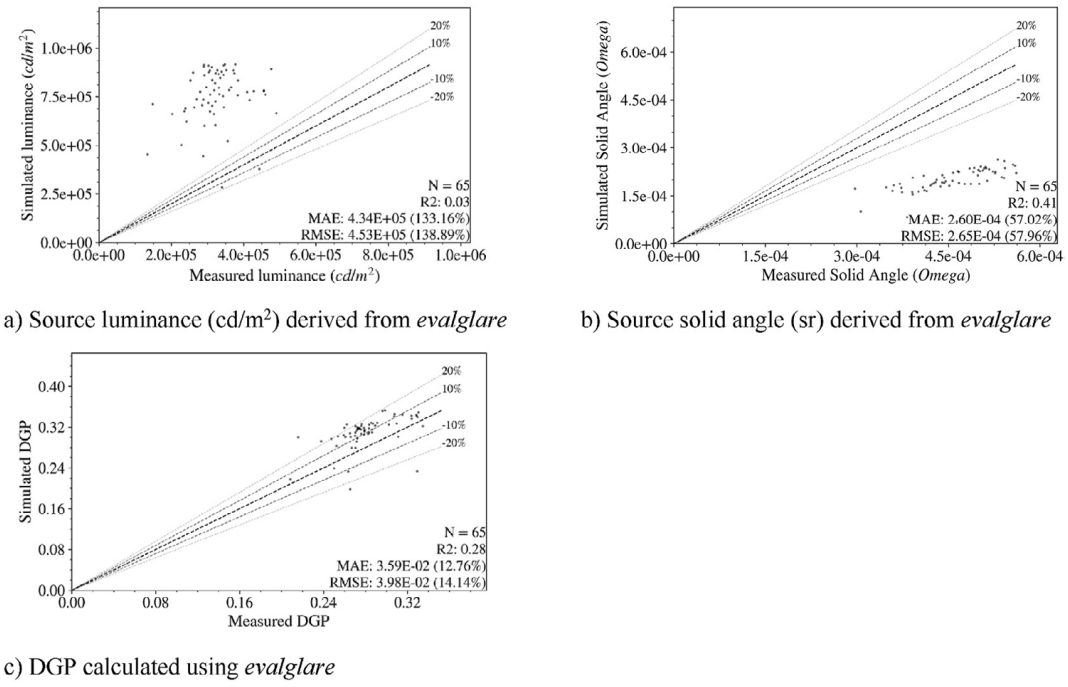

a) Source luminance (cd/m²) derived from *evalglare*

b) Source solid angle (sr) derived from *evalglare*

c) DGP calculated using *evalglare*

Fig. 26. *Evalglare* data derived from measured (x-axis) and simulated HDR images (y-axis): a) source luminance (cd/m^2), b) source solid angle (sr), and c) DGP. Simulated case: Anisotropic-k6, PE triggered, $\varphi_i < 90°$, with blur. Source: LBNL.

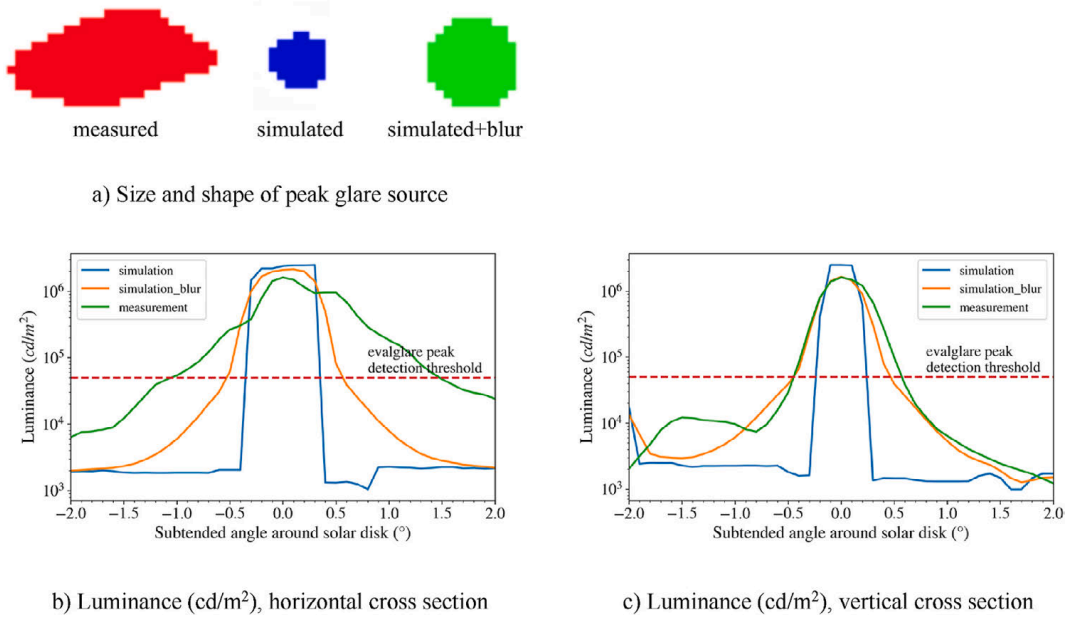

a) Size and shape of peak glare source

b) Luminance (cd/m²), horizontal cross section

c) Luminance (cd/m²), vertical cross section

Fig. 27. a) Illustration of the size and shape of the peak glare sources detected by *evalglare* from the measured and simulated HDR images, where luminance of sources (left to right): 318,922 cd/m^2, 1,828,053 cd/m^2, and 783,944 cd/m^2; b) luminance profiles taken in the horizontal cross section; and c) vertical cross section. Case: Anisotropic-k6, March 11, 13:05. Source: LBNL.

3.3.3). Larger errors occurred at more oblique angles of incidence, due in part to noisy triggering of the PE algorithm.

- When discomfort glare was evaluated for periods when there was specular transmission (PE triggered), the solid angle of the simulated glare source was smaller and thus its intensity was higher than that of the measured glare source, resulting in simulated DGP values that were greater (i.e., more conservative) than measured values (Section 4.2.5).

The pilot validation provided insights into sources of error across the entire workflow:

- There are inherent limitations associated with goniophotometric measurements (delineated in Section 3.1) and practical limits of backwards ray tracing. Even if we were able to measure at near-specular directions with resolutions far below 0.5°, random (ambient) sampling of such tabulated BSDF models would not be feasible. Getting the corresponding resolution of ambient rays of approximately $(180°/0.5°)^2$ would require setting the Radiance *–ad* parameter to 130000 and higher. The problem of missing near-

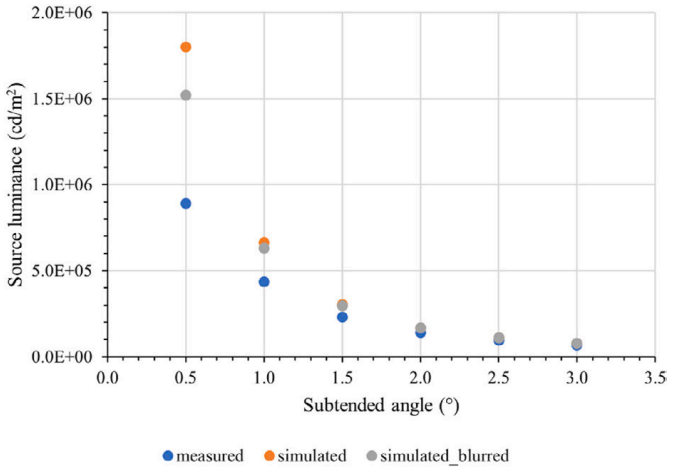

Fig. 28. Source luminance (cd/m^2) as a function of subtended angle centered on the solar disk. Case: Anisotropic-k6, March 11, 13:05. Source: LBNL.

specular data arises from the validation of the peak shape reconstruction in the image domain (i.e., the point spread function filter). The peak extraction algorithm addresses both of these limitations.

- The PE algorithm's representation of near specular and specular scattering of high-intensity sunlight can be within acceptable limits if adequate goniophotometer measurements are made to capture the characteristics of the material (e.g., anisotropic with bilateral symmetry). In this study, luminance remained low in other parts of the scene (<2000 cd/m^2), indicating good trends in energy conservation.
- The basis resolution of the tabulated BSDFs can affect when peak extraction is triggered. As a result, simulated source luminance levels vary with basis resolution. In general, higher resolution bases yield greater accuracy up to a limit; the basis resolution that yields lowest error must be determined through sensitivity analysis. This dependency is due to instability in the peak extraction method, which is exacerbated by the variability of the measurements, interpolation, and representation (cf. Section 3.3.3). We can miss the peak in some cases, underestimate it sometimes, and overestimate it other times. This is illustrated in Fig. 30, where the peak of the tensor tree dataset is not particularly stable as it changes in size and maximum value in ways that are probably not seen in the original data. Most of this variability likely comes from converting to a finite sampling representation (basis).
- The tabulated BSDF with the PE algorithm is limited in its ability to model the shape of the sun's glare source, leading to discrepancies between measured and simulated source luminance, and over- and under-estimation of glare discomfort when specular or partial specular transmission does or does not occur, respectively. Simulated glare discomfort is likely to be conservative under sunny conditions, but further modifications are needed to improve modeling accuracy.

5.2. Assessment of errors on DGP accuracy

This analysis focused on prediction accuracy of vertical illuminance and source luminance as inputs to any arbitrary metric (i.e., any daylight discomfort glare metric), but evaluates simulated performance for the DGP metric specifically. The DGP metric combines saturation glare (represented by the vertical illuminance term (E_v)) and contrast glare (represented by the glare source luminance (L_s) divided by E_v, by source solid angle (ω), and by the position of the glare source within the field of view (P)), see Equation (1).

$$\mathrm{DGP} = \underbrace{c_1 \cdot E_v}_{\text{saturation term}} + \underbrace{c_2 \cdot \log_{10}\left(1 + \sum_{i=1}^{n} \frac{L_{s,i}^2 \omega_{s,i}}{E_v^{1.87} P_{s,i}^2}\right)}_{\text{contrast term}} + c_3) \quad (1)$$

For the investigated case, the sun as glare source is a significant factor in the perception of glare, since the low hemispherical transmittance of the fabric (around 1%) leads to E_v in the range of less than 500 lx (i.e., saturation glare is not dominant). For that reason, the contrast term in the DGP equation (ref. to Equation (1)) becomes dominant.

An intrinsic problem of all contrast glare metrics/terms is the non-linearity between the predicted glare sensation (typically a function of $L^2 * \omega$) and the energy of the glare source received by the eye (function of

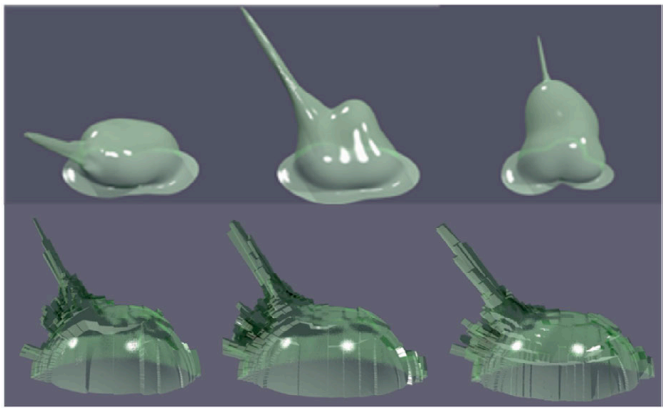

Fig. 30. Upper row: BSDF produced by the interpolant showing the distribution of the specular, semi-specular, and diffusely scattered outgoing flux for varying angles of incidence. Lower row: Tabulated BSDF with a –k6 tensor tree resolution for the same fabric. Both sets of images are shown in logarithmic scale.

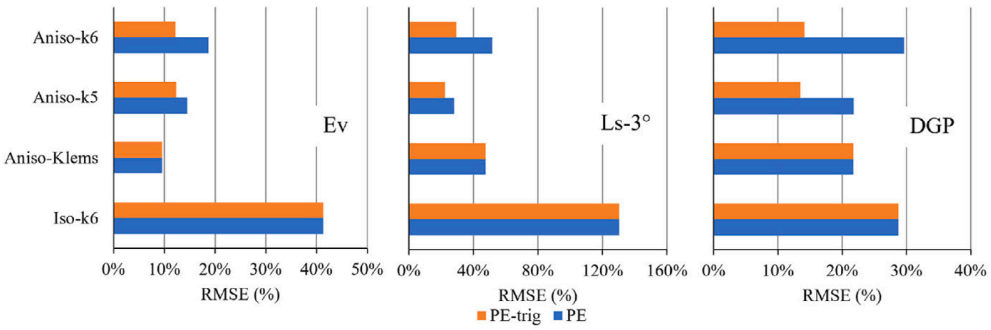

Fig. 29. RMSE (%) values for vertical illuminance (top), source luminance for 3° cone (middle), and DGP (bottom). BSDF cases (left to right): isotropic-k6, anisotropic-Klems, anisotropic-k5, and anisotropic-k6 with PE (blue) or PE triggered (orange). Data given for $\varphi_i < 90°$. Source: LBNL. (For interpretation of the references to color in this figure legend, the reader is referred to the Web version of this article.)

L *ω). As a consequence, it becomes important to match the luminance *and* the solid angle at the same time – just conserving energy leads to a mismatch when one of the variables deviates.

A potential difference of the solid angle can occur because of the blur of the sun disk in measured HDR images versus ideal sun disk simulations. Simulations might overestimate DGP because DGP was developed using HDR imaging and this underlying data includes the camera lens flare, increasing sun-disk size. For this reason, a filter based on a Lorentzian function was developed in this study and applied to all images. For other metrics that did not use HDR imaging in their derivation (e.g., daylight glare index (DGI)), the filter may not apply. Further work is needed to develop a general method for deriving this filter.

A study on *evalglare* parameter settings [52] revealed the challenges of heuristic glare source identification methods (i.e., task area, threshold, factor method) and dependency of these methods on the luminance distribution within the measured scene (i.e., subjective response in scenes dominated by contrast versus saturation glare). Further user assessments are needed in conditions where small, high-intensity daylight glare sources are within the field of view in order to confirm the validity of existing glare metrics like DGP. Until then, it is unclear what are acceptable levels of error for inputs to discomfort glare metrics.

5.3. Potential solutions to improve accuracy

When PE is triggered, tabular BSDFs with higher resolution yielded lower levels of error when predicting DGP. Alternatively, if the PE algorithm is not used, then higher resolution BSDFs are expected to yield more accurate results. It should be possible to enable higher-resolution tensor trees in the non-PE case by fixing memory issues associated with dense sampling, either using an out-of-core algorithm, or clever inline pruning methods. We would also need to solve the problem associated with storing Monte Carlo inversion tables at high resolution, which are created during the ray-tracing simulation, and can overwhelm virtual memory in some cases. We recently added a least-recently-used cache purging algorithm to address this problem, but it should be balanced carefully against memory size for optimum performance.

The specification of the appropriate BSDF resolution for different shading and daylighting systems in connection with the targeted evaluation metrics is the subject of current research. Increasing the BSDF resolution might lead to practical problems in handling the data in simulation software. Decreasing the average patch sizes down to about 0.5° (e.g., tensor tree k = 8 to k = 9, cf. Table 1) leads to the same issues in a backward Monte Carlo ray tracing algorithm: finding hotspots in the exiting distribution is challenging, similar in the challenge of finding the sun disk (the latter can efficiently be avoided with a deterministic approach targeting the known position of the sun [53]). In addition, we know that lower resolution BSDF data is likely adequate for evaluating illuminance-based annual metrics such as daylight autonomy [54]. For some classes of fenestration systems, the Klems basis with sufficient underlying measured data together with the application of the peak extraction algorithm could be an adequate solution.

While increasing the model resolution to improve accuracy in the case of direct transmission seems possible, refined methods to measure the BSDF at near-specular directions may be an alternate solution. This can, to some degree, be accomplished by a smaller detector aperture and the use of light sources that produce a narrower and less diverging beam, but maintain the beam integral. To mitigate the impact on acquisition times, this refinement could be limited to the measurement of the near-specular region. A wider illumination and larger detector aperture could rapidly acquire the diffuse background, resulting in an increased signal in regions of low, diffuse scatter. Such a modification would provide an instrument configuration optimized for the evaluated class of fabrics, featuring high direct and low diffuse transmission. Another potential solution to the problematic measurement of the near-specular peak, that avoids such interventions in the instrumentation, may be to evaluate the measured BSDF in conjunction with the known instrument signature by deconvolution techniques.

5.4. View

One of the difficulties of general simulation using BSDF data is that it does not directly represent view properly. Besides failing to show the view out the window, the simulation of direct sunlight and reflections visible through such systems is compromised with a finite BSDF representation. The method of peak extraction is a workable solution to this problem that semi-automatically determines an appropriate view component from measured BSDF data.

In terms of view clarity [55,56], PE generally undermines these calculations since it automatically discounts near specular scattering in the vicinity of a strong peak. For such cases, it would be better to obtain a high-resolution BSDF and do the analysis without peak extraction. To model outdoor objects with sufficient resolution for edge detection algorithms, the resolution of the BSDF would also need to be increased (e.g., k = 9). Interreflections within the material itself, in the case of direct sunlight, and between the window glass and shade would be incorporated using genBSDF if the shade is interior to the window glass but would require alternate use of genBSDF (+forward -backward) if the glass was on the interior of the shade. This view aspect was not evaluated in this study and should be addressed in future evaluations.

5.5. Applicability

The PE algorithm evaluated in this study is only applicable to forward scattering materials with transmission that is regular (i.e., some openness fraction where no scattering occurs in and around the line of sight from the source, e.g. fabrics, fritted glass, direct transmission in between Venetian blinds). Reflected or refracted peaks are not extracted by the current PE algorithm. Linear structures that deflect light into a broad vertical region may be best modeled with a high resolution BSDF without PE. PE could be used to model regular transmission that occurs through the space between curved mirror blind slats but not the mirrored slats themselves. Frosted glass transmits light in a broad, near-Lambertian lobe, so while the term “specular” transmission is used by some to describe its properties, the PE algorithms in this study would not be applicable. A high resolution BSDF without PE may be applicable but simulations are subject to noise and are less efficient as discussed in Section 3.3. Further validation is needed to evaluate performance of both non-PE and PE methods for these systems.

If off-specular and upward-reflected peaks are expected, the method of photon mapping with high-resolution BSDFs [53] is recommended. Photon mapping in this case adds the benefits of forward raytracing for small and high intensity light sources (e.g., the sun) to the general backward raytracing functionality. Though still limited by the resolution of the BSDF data for sharpness of specularly reflected light, reflected peaks can be simulated more efficiently and with reduced noise.

An international expert group within the International Energy Agency Solar Heating and Cooling Programme Task 61/EBC Annex 77: Integrated Solutions for Daylighting and Electric [57] is addressing standardization of BSDF daylight system characterization and aiming at the development of a general guideline for the generation of BSDF data sets.

6. Conclusions

Based on a pilot validation study, a general method developed to generate and use data-driven BSDFs was determined to be yield satisfactory levels of accuracy in the determination of vertical illuminance and source luminance for daylighting and shading systems that allow specular and near specular transmission. Prediction of discomfort glare was conservative under worst case sunny conditions but further work is needed to reduce errors.

Declaration of competing interest

The authors declare that they have no known competing financial interests or personal relationships that could have appeared to influence the work reported in this paper.

Acknowledgments

This work was supported by the Assistant Secretary for Energy Efficiency and Renewable Energy, Building Technologies Office of the U.S. Department of Energy under Contract No. DE-AC02-05CH11231 and by the California Energy Commission under the Electric Program Investment Charge (EPIC) Program, Solicitation Number: PON-13-301, entitled "Developing A Portfolio of Advanced Efficiency Solutions: Technologies and Approaches for More Affordable and Comfortable Buildings", that was awarded to Lawrence Berkeley National Lab for the work herein.

The Lucerne University of Applied Sciences and Arts, Lucerne School of Engineering and Architecture, Competence Centre Building Envelope and Structural Engineering was supported by the Swiss Federal Office of Energy SFOE (#SI501427-01) as part of the project "High Resolution Complex Glazing Library (BIMSOL)", and by the Swiss Innovation Agency Innosuisse as part of the Swiss Competence Center for Energy Research SCCER FEEB&D.

Bartenbach GmbH, Aldrans, Austria, received funding through the project „Early Stage: Tageslicht-Blendung und Virtual Reality" financed the Austrian Research Promotion Agency FFG.

École Polytechnique Fédérale de Lausanne (EPFL), Architecture, Civil and Environmental Engineering (ENAC), Laboratory of Integrated Performance in Design (LIPID) supported this study.

The authors thank Peter Apian-Bennewitz for continuously sharing his expertise in BSDF measurements, that supported the development of the modelling technique as well as the interpretation of results.

Appendix A

Radiance convention for phi and theta angles

The Radiance convention for phi (φ) and theta (θ) angles was used in this study (Fig. A1), where the "front" (F symbol) of the sample faces towards the indoors (inward surface normal z-axis); i.e.,

- $\theta_i = 0°–90°$ for incident angles and $\theta_s = 90°–180°$ for outward scattering angles, measured from the inward z-axis;
- φ_i and φ_s are measured from the x-axis in the x-y plane, where $\varphi = 0°$ points horizontally to the right and $\varphi = 90°$ points upwards when viewing the front of the sample.

For example, the sun with an altitude of 60° at noon would have an incident angle (i) of $\theta_i = 150°$ and $\varphi_i = 90°$ on a south facing window with the front of the roller shade fabric facing towards the indoors.

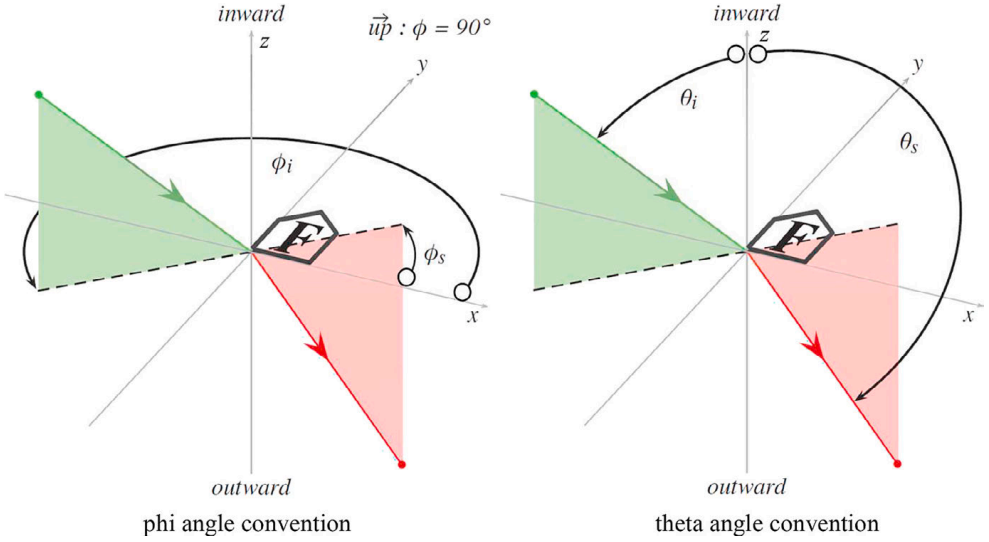

Fig. A1. Radiance convention for BSDF coordinates, phi and theta. Source: HSLU.

Definition of isotropic and anisotropic materials

Isotropic materials exhibit the same scattering behavior irrespective of sample rotation. Anisotropic materials exhibit varying scattering behavior, where the material can be symmetric over a single axis (bilateral), over two axes (quadrilateral), or unsymmetric (e.g., random pattern of colors and/or weave across plane of fabric). For isotropic materials, goniophotometer measurements at one phi and several theta angles of incidence are needed. For anisotropic materials, measurements at multiple phi and theta angles are needed. (See Fig. A2)

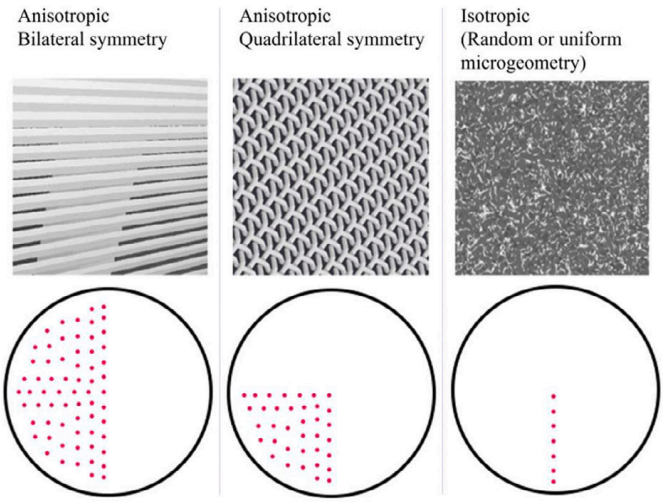

Fig. A2. Diagram illustrating anisotropic and isotropic materials (above) and measurement points for phi and theta angles (below) that would be necessary to characterize the scattering properties of the material. Source: Anyhere Software.

References

[1] G.B. Smith, C.G. Granqvist, Green Nanotechnology: Solutions for Sustainability and Energy in the Built Environment, CRC, Boca Raton, FL, 2010.

[2] M.M. Grasso, B.D. Hunn, A.M. Rewerts, Effect of textile properties in evaluating a directional shading fabric, Textil. Res. J. 67 (4) (1997) 233–247.

[3] G. Mbise, G.B. Smith, G.A. Niklasson, C.G. Granqvist, December. Angular selective window coatings: theory and experiment, in: Optical Materials Technology for Energy Efficiency and Solar Energy Conversion VIII, vol. 1149, International Society for Optics and Photonics, 1989, pp. 179–200.

[4] A. Shehabi, N. DeForest, A. McNeil, E. Masanet, J. Greenblatt, E.S. Lee, G. Masson, B.A. Helms, D.J. Milliron, US energy savings potential from dynamic daylighting control glazings, Energy Build. 66 (2013) 415–423.

[5] R. Capperucci, R.C. Loonen, J.L. Hensen, A.L. Rosemann, Angle-dependent optical properties of advanced fenestration systems—finding a right balance between model complexity and prediction error, in: Building Simulation, Tsinghua University Press, 2018, pp. 1–15.

[6] Department of Energy (DOE), U.S, Buildings Energy Databook, Energy Efficiency & Renewable Energy Department, 2011.

[7] C. Gehbauer, D.H. Blum, T. Wang, E.S. Lee, An assessment of the load modifying potential of model predictive controlled dynamic facades within the California context, Energy Build. 210 (2020) 109762.

[8] P.R. Tregenza, I. Waters, Daylight coefficients, Light. Res. Technol. 15 (2) (1983) 65–71.

[9] J. Mardaljevic, Simulation of annual daylighting profiles for internal illuminance, Light. Res. Technol. 32 (3) (2000) 111–118.

[10] C.F. Reinhart, S. Herkel, The simulation of annual daylight illuminance distributions — a state-of-the-art comparison of six RADIANCE-based methods, Energy Build. 32 (2000) (2000) 167–187.

[11] C.F. Reinhart, O. Walkenhorst, Validation of dynamic RADIANCE-based daylight simulations for a test office with external blinds, Energy Build. 33 (7) (2001) 683–697, 2001.

[12] J.H. Klems, A new method for predicting the solar heat gain of complex fenestration systems: I. Overview and derivation of the matrix layer calculation, Build. Eng. 100 (1) (1994) 1065–1072.

[13] M. Saxena, G. Ward, T. Perry, L. Heschong, R. Higa, Dynamic Radiance – predicting annual daylighting with variable fenestration optics using BSDFS, in: Fourth National Conference of IBPSA-USA, New York City, New York, August 11 – 13, 2010, 2010.

[14] G. Ward, R. Mistrick, E.S. Lee, A. McNeil, J. Jonsson, Simulating the daylight performance of complex fenestration systems using bidirectional scattering distribution functions within Radiance, Leukos 7 (4) (2011) 241–261.

[15] A. McNeil, The five-phase method for simulating complex fenestration with Radiance. https://facades.lbl.gov/sites/all/files/tutorial-fivephasemethod.pdf, 2013. (Accessed 15 January 2021).

[16] David Geisler-Moroder, Eleanor S. Lee, Gregory J. Ward, Validation of the five-phase method for simulating complex fenestration systems with Radiance against field measurements, in: Proceedings of Building Simulation 2017, International Building Performance Simulation Association, San Francisco, August 7-9, 2017.

[17] T. Wang, G. Ward, E.S. Lee, Efficient modeling of optically-complex, non-coplanar exterior shading: validation of matrix algebraic methods, Energy Build. 174 (2018) 464–483.

[18] L.O. Grobe, Photon-mapping in climate-based daylight modelling with high-resolution BSDFs, Energy Build. 205 (2019) 109524.

[19] Attachments Energy Rating Council, "AERC 1.1, procedures for determining the optical and thermal properties of window attachment materials", version 1.3, Appendix C, https://aercnet.org/product/aerc-1-1-procedures-determining-optical-thermal-properties-window-attachment-materials/, 2018. (Accessed 15 January 2021).

[20] P. Shirley, K. Chiu, A low distortion map between disk and square, J. Graph. Tool. 2 (3) (1997) 45–52.

[21] T. Tongbuasirilai, J. Unger, J. Kronander, M. Kurt, Compact and intuitive data-driven BRDF models, Vis. Comput. (36) (2020) 855–872.

[22] F.E. Nicodemus, J.C. Richmond, J.J. Hsia, I.W. Ginsberg, T. Limperis, Geometrical Considerations and Nomenclature for Reflectance, US Department of Commerce, National Bureau of Standards, 1977.

[23] J.C. Stover, Optical Scattering: Measurement and Analysis, Society of Photo-Optical Instrumentation Engineers, 2012.

[24] P. Apian-Bennewitz, Review of Simulating Four Classes of Window Materials for Daylighting with Non-standard BSDF Using the Simulation Program Radiance, 2013 arXiv preprint arXiv:1307.4214.

[25] BME, Building material examples (BME) BSDF, BRDF data and models. http://www.pab.eu/gonio-photometer/demodata/bme, 2020. (Accessed 15 January 2021).

[26] J.C. Jonsson, E.S. Lee, M. Rubin, August. Light-scattering properties of a woven shade-screen material used for daylighting and solar heat-gain control, in: Reflection, Scattering, and Diffraction from Surfaces, vol. 7065, International Society for Optics and Photonics, 2008, p. 70650R.

[27] A. McNeil, C.J. Jonsson, D. Appelfeld, G. Ward, E.S. Lee, A validation of a ray-tracing tool used to generate bi-directional scattering distribution functions for complex fenestration systems, Sol. Energy 98 (2013) (2013) 404–414.

[28] H. Aydinli, H. Kaase, Measurement of luminous characteristics of daylighting materials, technical report, in: International Energy Agency Solar Heating and Cooling Programme (IEA SHC) Task 21, 1999, p. 1999.

[29] G. Ward Larson, R. Shakespeare, Rendering with Radiance: the Art and Science of Lighting Visualization, Morgan Kaufmann, San Francisco, 1998.

[30] E.S. Lee, D. Geisler-Moroder, G. Ward, Modeling the direct sun contribution in buildings using matrix algebraic approaches: methods and validation, Sol. Energy 160 (2018) 380–395.

[31] D. Geisler-Moroder, E.S. Lee (Eds.), White Paper on BSDF Generation Procedures for Daylighting Systems, T61.C.2.1 – A Technical Report of Subtask C, International Energy Agency Solar Heating & Cooling Programme, Task 61/EBC Annex 77, Integrated Solutions for Daylighting and Electric Lighting: from Component to User Centered System Efficiency, 2021.

[32] M. Krehel, J.H. Kämpf, S. Wittkopf, Characterisation and modelling of advanced daylight redirection systems with different goniophotometers, in: CISBAT 2015 International Conference on Future Buildings and Districts – Sustainability from Nano to Urban Scale, Lausanne, Switzerland, September 9-11, 2015, vol. 1, 2015.

[33] C. Schwanengel, Gegenüberstellung von Messtechniken zur Messung von Lichtstärkeverteilungen und Lichtstärkeverteilungsausschnitten, TechnoTeam Bildverarbeitung GmbH, 2010, p. 34. August 2010, Table 3.1.

[34] L.O. Grobe, S. Wittkopf, P. Apian-Bennewitz, J.C. Jonsson, M.D. Rubin, Experimental validation of bidirectional reflection and transmission distribution measurements of specular and scattering materials, Proc. SPIE 7725 (2010) 772510.

[35] B. Karamata, M. Andersen, A Review and Analysis of Parallel Goniophotometry. LUX EUROPA 2013, Krakow, Poland, September 17-19, 2013.

[36] P. Apian-Bennewitz, New scanning gonio-photometer for extended BRTF measurements, in: Proc. SPIE 7792, 2010, p. 77920O. Reflection, Scattering, and Diffraction from Surfaces II, September 1, 2010.

[37] N. Bonneel, M. van de Panne, S. Paris, W. Heidrich, Displacement interpolation using Lagrangian mass transport, in: ACM Transactions on Graphics – Proceedings of ACM SIGGRAPH Asia 2011, vol. 30, 2011, pp. 1–12 (6), Article 158.
[38] G. Ward, M. Kurt, N. Bonneel, A Practical Framework for Sharing and Rendering Real-World Bidirectional Scattering Distribution Functions, LBNL-5954E, Lawrence Berkeley National Laboratory, Berkeley, CA, 2012. September 2012.
[39] G. Ward, M. Kurt, N. Bonneel, Reducing anisotropic BSDF measurement to common practice, in: Proceedings of the Eurographics 2014 Workshop on Material Appearance Modeling: Issues and Acquisition, Lyon, France, June 25, 2014, 2014, pp. 5–8.
[40] J. Wienold, Evalglare version 2.0. École Polytechnique Fédérale de Lausanne. https://www.radiance-online.org/community/workshops/2016-padua/presentations/211-Wienold-Evalgaare2.0.pdf, 2016. (Accessed 15 January 2021).
[41] J. Wienold, J. Christoffersen, Evaluation methods and development of a new glare prediction model for daylight environments with the use of CCD cameras, Energy Build. 38 (7) (2006) 743–757.
[42] J. Wienold, T. Iwata, M. Sarey Khanie, E. Erell, E. Kaftan, R.G. Rodriguez, J. A. Yamin Garretón, T. Tzempelikos, I. Konstantzos, J. Christoffersen, T.E. Kuhn, Cross-validation and robustness of daylight glare metrics, Light. Res. Technol. 51 (7) (2019) 983–1013.
[43] Y.R. Yang, J. Wanek, M. Shahidi, Representing the retinal line spread shape with mathematical functions, J. Zhejiang Univ. - Sci. B 9 (12) (2008) 996–1002.
[44] J.C. Jonsson, C. Curcija, H.R. Wilson, J. Slack, S. Appert, M. Quinones, S. Zhao, K. Wu, M. Rubin, Measurement Procedure for Optical and Thermophysical Properties of Fenestration Shading Fabrics to Be Used in WINDOW, Lawrence Berkeley National Laboratory, Berkeley, CA, June 13, 2018.
[45] N.A. Kotey, J.L. Wright, et al., Determining off-normal solar optical properties of roller blinds, Build. Eng. 115 (1) (2009) 145–154.
[46] P. Apian-Bennewitz, J. von der Hardt, Enhancing and calibrating a goniophotometer, Sol. Energy Mater. Sol. Cell. 54 (1998) 309–322.
[47] E. Brembilla, D.A. Chi, C.J. Hopfe, J. Mardaljevic, Evaluation of climate-based daylighting techniques for complex fenestration and shading systems, Energy Build. 203 (2019) 109454.
[48] C. Pierson, C. Cauwerts, M. Bodart, J. Wienold, Tutorial: luminance maps for daylighting studies from high dynamic range photography, Leukos (2020), https://doi.org/10.1080/15502724.2019.1684319.
[49] R. Perez, R. Seals, J. Michalsky, All-weather model for sky luminance distribution—preliminary configuration and validation, Sol. Energy 50 (3) (1993) 235–245.
[50] Gendaylit, Radiance manual. https://www.radiance-online.org/learning/documentation/manual-pages/pdfs/gendaylit.pdf, 2019. (Accessed 15 January 2021).
[51] G. Ward, The Radiance 5.1 synthetic imaging system. https://floyd.lbl.gov/radiance/refer/refman.pdf, 2018. (Accessed 15 January 2021).
[52] C. Pierson, J. Wienold, M. Bodart, Daylight discomfort glare evaluation with *evalglare*: influence of parameters and methods on the accuracy of discomfort glare prediction, Buildings 8 (2018) 94, 2018.
[53] L.O. Grobe, Photon mapping in image-based visual comfort assessments with BSDF models of high resolution, J. Build. Perform. Simul. 12 (6) (2019) 745–758.
[54] A. McNeil, On the Sensitivity of Daylight Simulations to the Resolution of the Hemispherical Basis Used to Define Bidirectional Scattering Distribution Functions, DOE/LBNL FY11 Technical Report, 2011.
[55] I. Konstantzos, Y.C. Chan, J.C. Seibold, A. Tzempelikos, R.W. Proctor, J. B. Protzman, View Clarity Index: a new metric to evaluate clarity of view through window shades, Build. Environ. 90 (2015) 206–214.
[56] W. Ko, G. Brager, S. Schiavon, S. Selkowitz, Building Envelope Impact on Human Performance and Well-Being: Experimental Study on View Clarity, Center for the Built Environment, UC Berkeley, 2017. Retrieved from, https://escholarship.org/uc/item/0gj8h384.
[57] IEA, IEA SHC task 61/EBC Annex 77: integrated solutions for daylighting and electric lighting: from component to user centered system efficiency. http://task61.iea-shc.org/, 2019. (Accessed 15 January 2021).